

Lawrence Berkeley National Laboratory

LBL Publications

Title

ADDGALS: Simulated Sky Catalogs for Wide Field Galaxy Surveys

Permalink

<https://escholarship.org/uc/item/9dq300d0>

Journal

The Astrophysical Journal, 931(2)

ISSN

0004-637X

Authors

Wechsler, Risa H
DeRose, Joseph
Busha, Michael T
[et al.](#)

Publication Date

2022-06-01






DOI

10.3847/1538-4357/ac5b0a

Peer reviewed



ADDGALS: Simulated Sky Catalogs for Wide Field Galaxy Surveys

Risa H. Wechsler^{1,2,3} , Joseph DeRose⁴ , Michael T. Busha^{2,7}, Matthew R. Becker⁵ , Eli Rykoff^{2,3} , and August Evrard⁶ ¹Department of Physics, Stanford University, 382 Via Pueblo Mall, Stanford, CA 94305, USA²Kavli Institute for Particle Astrophysics & Cosmology, P.O. Box 2450, Stanford University, Stanford, CA 94305, USA³SLAC National Accelerator Laboratory, Menlo Park, CA 94025, USA⁴Lawrence Berkeley National Laboratory, 1 Cyclotron Road, Berkeley, CA 93720, USA⁵High-Energy Physics Division, Argonne National Laboratory, Lemont, IL 60439, USA⁶Departments of Physics and Astronomy, University of Michigan, Ann Arbor, MI, USA

Received 2021 June 4; revised 2022 February 20; accepted 2022 March 3; published 2022 June 3

Abstract

We present a method for creating simulated galaxy catalogs with realistic galaxy luminosities, broadband colors, and projected clustering over large cosmic volumes. The technique, denoted ADDGALS (Adding Density Dependent GALaxies to Lightcone Simulations), uses an empirical approach to place galaxies within lightcone outputs of cosmological simulations. It can be applied to significantly lower-resolution simulations than those required for commonly used methods such as halo occupation distributions, subhalo abundance matching, and semi-analytic models, while still accurately reproducing projected galaxy clustering statistics down to scales of $r \sim 100 h^{-1} \text{kpc}$. We show that ADDGALS catalogs reproduce several statistical properties of the galaxy distribution as measured by the Sloan Digital Sky Survey (SDSS) main galaxy sample, including galaxy number densities, observed magnitude and color distributions, as well as luminosity- and color-dependent clustering. We also compare to cluster–galaxy cross correlations, where we find significant discrepancies with measurements from SDSS that are likely linked to artificial subhalo disruption in the simulations. Applications of this model to simulations of deep wide-area photometric surveys, including modeling weak-lensing statistics, photometric redshifts, and galaxy cluster finding, are presented in DeRose et al., and an application to a full cosmology analysis of Dark Energy Survey (DES) Year 3 like data is presented in DeRose et al. We plan to publicly release a 10,313 square degree catalog constructed using ADDGALS with magnitudes appropriate for several existing and planned surveys, including SDSS, DES, VISTA, Wide-field Infrared Survey Explorer, and Rubin Observatory’s Legacy Survey of Space and Time.

Unified Astronomy Thesaurus concepts: [Cosmology \(1313\)](#); [Dark matter \(353\)](#); [N-body simulations \(1083\)](#); [Large-scale structure of the universe \(902\)](#); [Galaxy dark matter halos \(1880\)](#); [Galaxy evolution \(594\)](#)

1. Introduction

Cosmology and the study of galaxy formation are undergoing a renaissance driven by exponential increases in computing power, the public availability of large amounts of high-quality sky survey data, and continued investment in ever-more sensitive instrumentation. These trends place stringent demands on the accuracy of the theoretical models used to analyze such survey data.

The best current models of the universe posit that hierarchical structure formation via the gravitational collapse of cold dark matter drives the formation and evolution of galaxies. Simultaneously, galaxies serve as a rich set of tracers of the cosmic density and velocity fields, imparting the galaxy distribution with sensitivity to fundamental physics like cosmic acceleration, modifications to General Relativity, massive neutrinos, and the microphysical nature of dark matter (e.g., Weinberg et al. 2013). This rich discovery potential demands precise connection between the galaxy and matter distributions, particularly on small cosmic scales, which hold immense statistical information. The galaxy–dark matter connection is a

key source of theoretical uncertainty in galaxy survey analyses concerned with constraints on fundamental physics.

The context above is driving two important trends in cosmology. First, researchers are developing a wealth of methods that aim to infer the connection between galaxies and their dark matter halos (see Wechsler & Tinker 2018 for a review). These studies usually employ large-volume, high-resolution N -body simulations of structure formation. Second, cosmologists now routinely employ “synthetic” or “mock” catalogs of galaxies to support analyses of survey data. These synthetic catalogs are constructed with a wide variety of techniques that draw from advances in understanding the connection between galaxies and halos. Published examples focusing on modeling galaxy populations in realistic survey lightcones include approaches using halo occupation distributions (HODs; Yan et al. 2004; Sousbie et al. 2008; Manera et al. 2013; Crocce et al. 2015; Fosalba et al. 2015; Smith et al. 2017; Harois-Déraps et al. 2018; Stein et al. 2020), semi-analytic models (SAMs; Eke et al. 2004; Cai et al. 2009; Merson et al. 2013; Somerville et al. 2021), subhalo abundance matching (SHAM; Gerke et al. 2013; Safonova et al. 2021), or a combinations of the above (Korytov et al. 2019) to accomplish this task.

In this work, we present ADDGALS (Adding Density-Determined Galaxies to Lightcone Simulations), a computationally inexpensive, but high-fidelity approach for constructing synthetic galaxy catalogs from lightcone simulations, designed to support the analysis of large-area galaxy survey

⁷ Present Address: Securiti.



data. Unlike HOD, SAM, and SHAM approaches, it is designed specifically to populate modest-resolution N -body simulations with galaxies that have realistic luminosities, spectral energy distributions (SEDs), and clustering. Except for a few percent of galaxies occupying the most massive halos, ADDGALS is not sensitive to these N -body simulations' lack of convergence at the smallest scales. The modest expense of these simulations enables the creation of large numbers of large-volume realizations of the universe, which are often required by modern survey analyses.

With its modest computational requirements, ADDGALS can be used to bring a new level of realism to survey analysis tasks that require a *statistical sample* of synthetic catalogs. Examples of these tasks include generating covariance matrices or testing the robustness of these analyses to key systematic effects through direct, end-to-end tests where the true answer is known. MacCrann et al. (2018) and DeRose et al. (2021b) presented key examples of the latter approach. These works combine the Dark Energy Survey (DES) year one (Y1) and year three (Y3) analysis pipelines with 18 synthetic catalogs produced with the methodology presented in this work to perform end-to-end tests of a 3×2 point weak lensing and galaxy clustering analysis. To et al. (2021) performed a similar analysis that combined these statistics with cluster counts and cluster–galaxy cross correlations. Due to the realism of the ADDGALS catalogs, they were able to use the same analysis pipeline as was applied to the DES data. These tests depended critically on simulated catalogs that jointly modeled several effects, including various observables (e.g., galaxy clustering, galaxy–galaxy lensing, cosmic shear, and cluster counts), photometric redshifts, and survey effects like varying depth maps. Further, tens of realizations were needed to demonstrate that the recovered parameters were accurate to well below the sensitivity of the DES measurements themselves. These kinds of tests will be increasingly important as surveys begin to produce stringent constraints on fundamental physics, motivating an approach that is able to model large volumes and multiple observables with modest computational cost.

1.1. Previous Approaches

As emphasized by Wechsler & Tinker (2018), currently used approaches for modeling galaxies within large-scale structure face trade-offs between the fidelity of the modeled properties, the resolution or computational requirements of the method, and the degree to which the model is physics-driven or empirically data-driven. For example, the SHAM approach, which assumes that all galaxies are placed on resolved halos and subhalos, has been shown to faithfully reproduce the spatial distribution of galaxies in the local universe where it can best be measured (Kravtsov et al. 2004; Reddick et al. 2013; Chaves-Montero et al. 2016; Lehmann et al. 2017; Contreras et al. 2021; DeRose et al. 2021a), as well as the evolution of the galaxy population with time (Conroy et al. 2006; Moster et al. 2011; Behroozi et al. 2013a), with a very small number of parameters. This technique has the advantage of including several important correlations between halo history, galaxy populations, and environment that are neglected by some other methods, but has stringent resolution requirements.

One of the most commonly used methods, populating simulations with galaxies using an HOD (e.g., Jing 1998;

Seljak 2000; Berlind & Weinberg 2002; Bullock et al. 2002; Yang et al. 2003; Zheng et al. 2005; Mandelbaum et al. 2006; van den Bosch et al. 2007; Zehavi et al. 2011; Zu & Mandelbaum 2015), places each galaxy in regions within resolved *host* halos, irrespective of dark matter substructures. This reduces the computational requirements on the simulations compared with methods that trace halo histories, but generally requires more parameters than abundance matching and may be missing relevant correlations between galaxy populations and halo history. The conditional luminosity function method (e.g., Yang et al. 2003; Cooray 2006) has similar requirements. The computational expense of HOD modeling can be further decreased by employing approximate, or low-resolution methods for generating halo catalogs (e.g., Bond & Myers 1996; Scoccimarro & Sheth 2002; Monaco et al. 2013; Tassev et al. 2013; White et al. 2014; Avila et al. 2015; Chuang et al. 2015; Kitaura et al. 2016; Izard et al. 2018; Balaguera-Antolínez et al. 2019; Feng et al. 2019).

SAMs (White & Frenk 1991; Kauffmann et al. 1993; Somerville & Primack 1999; Cole et al. 2000; Benson et al. 2002; Bower et al. 2006; Benson 2012; Guo et al. 2013; Croton et al. 2016) generally require a degree of resolution between abundance matching and the HOD—the former is more relevant if one wants to trace the histories of all galaxies properly and if one wants to keep every galaxy on a resolved substructure. This can be reduced to the less demanding requirements of the HOD if semi-analytic methods are used to track halo histories and the kinematics of satellite galaxies in larger systems (Benson 2012; Jiang & van den Bosch 2016; Yang et al. 2020; Jiang et al. 2021).

Concurrent with the development and use of the method described here, significant progress has been made in other data-driven approaches, particularly in empirical models that use information from halo histories. These approaches include extensions to the abundance matching approach like conditional abundance matching, which associates color or star formation rates with secondary halo properties (Hearin & Watson 2013; Masaki et al. 2013; Hearin et al. 2014; Yamamoto et al. 2015; Saito et al. 2016; Contreras et al. 2021) or that trace galaxy histories through the histories of their halos (e.g., Becker 2015; Moster et al. 2018; Behroozi et al. 2019) and constrain their properties with a wide range of data.

Finally, full-physics cosmological hydrodynamics methods (see Vogelsberger et al. 2020, for a recent review) are making steady progress in describing the galaxy–halo connection. A recent verification of three independent simulations examines the satellite galaxy occupation conditioned on total halo mass and redshift, finding a consistent form for the probability density function (PDF) along with slightly super-Poisson dispersion, but with mean counts varying by tens of percent (Anbajagane et al. 2020). These simulations are computationally expensive and thus challenging to use to model large survey volumes, but they can be used to inform HOD approaches and test SAM or empirical methods, and provide essential input into possible modification of the dark matter distribution from baryonic processes.

1.2. ADDGALS

ADDGALS' combination of realism and relatively low computational expense is due to a machine-learning style approach that uses higher-resolution N -body simulations to

train the galaxy–dark matter connection scales and data to train a physically motivated model for the dependence of galaxy properties on local density. This approach is similar in spirit to other recent works that employ statistical learning techniques to connect the dark matter distribution to the distribution of biased tracers (Modi et al. 2018; Berger & Stein 2019; Ramanah et al. 2019; Tröster et al. 2019; Zhang et al. 2019; Dai & Seljak 2021). The features that ADDGALS uses are chosen to be relatively insensitive to resolution effects in the simulations, while still encapsulating quantities relevant to the physics of galaxy formation.

A flowchart with the key steps of the algorithm is given in Figure 1. The ADDGALS algorithm can be divided into two main parts, the assignment of luminosities and the assignment of SEDs. In the first part, we fit a model to the distribution of galaxy absolute magnitude at fixed local overdensity using a high-fidelity model of the galaxy–halo connection. In this work, we use an SHAM model applied to high-resolution structure formation simulations, but this choice is not essential. We then use these distributions to populate a low-resolution simulation via Monte Carlo. This process is illustrated in steps 1 through 3 in the flowchart. In the second part of the ADDGALS algorithm, we use a conditional abundance matching model fit to the Sloan Digital Sky Survey (SDSS) in DeRose et al. (2021a) to assign an SED to each galaxy. Finally, we apply observational effects to produce the complete catalog. These parts correspond to steps 4 and 5 in the flowchart.

We demonstrate that these steps are able to reproduce the absolute magnitude dependent two-point clustering and halo occupation properties of the SHAM catalog. Further, we show that they reproduce a number of additional observed properties of SDSS galaxies, including their color distributions at a given absolute magnitude and the qualitative trends of the observed color-dependent clustering.

The model that is perhaps most similar to the one presented in this work is GALSAMPLER (Hearin et al. 2020), in that it places galaxies from a high-fidelity model of galaxy formation run on high-resolution simulations into the halos of lower-resolution simulations. The main distinguishing factor is the use of halo mass as the conditional variable in GALSAMPLER, whereas ADDGALS uses local Lagrangian density, which can be measured in significantly lower-resolution simulations.

In this work, ADDGALS is trained on an SHAM model, but the machine-learning style approach taken by ADDGALS generalizes to training on other models of the galaxy–halo connection, including hydrodynamical simulations, SAMs, or empirical models that trace halo histories. Note that it is likely that secondary properties of the density field will be needed for these generalizations in analogy to secondary halo properties and assembly bias. This flexibility combined with modest computational requirements will enable the production of suites of synthetic catalogs with different underlying models for the galaxy–halo connection. These suites can then be used to test the robustness of cosmological constraints from surveys to underlying assumptions about galaxy formation.

ADDGALS has been in use for some time to facilitate a variety of applications of large-scale sky survey data, with a particular focus on wide-area photometric surveys. A preliminary description of the work was presented in Wechsler (2004). Subsequent work using these catalogs has made use of earlier versions than those described here; in most cases, the

important details were described in those papers. Because of the ability of these techniques to accurately model large, wide surveys including realistic photometry and lensing, the range of applications has been broad.

Catalogs produced with this method have been used extensively in the testing, systematics assessment, and co-analysis of galaxy cluster catalogs and results with the MAXBCG and REDMAPPER algorithms (Becker et al. 2007; D. E. Johnston & Sheldon et al. 2007; in preparation; Koester et al. 2007a, 2007b; Rozo et al. 2007a, 2007b; Hansen et al. 2009; Sheldon et al. 2009; Tinker et al. 2012; Dietrich et al. 2014; Farahi et al. 2016; Varga et al. 2019; Abbott et al. 2020), for the improvement and testing of other galaxy cluster finders (Miller et al. 2005; Dong et al. 2008; Hao et al. 2010; Soares-Santos et al. 2011; Bleem et al. 2015), for the development and testing of a number of photometric redshift algorithms, especially in the context of DES (Gerdes et al. 2010; Cunha et al. 2012, 2014; Bonnett et al. 2016; Leistedt et al. 2016; Cawthon et al. 2018; Gatti et al. 2018; Hoyle et al. 2018; Buchs et al. 2019; Cawthon et al. 2020; Gatti et al. 2022; Myles et al. 2021) and Rubin Observatory’s Legacy Survey of Space and Time (LSST; Malz et al. 2018; Schmidt et al. 2020), for the development of various survey analysis approaches using weak-lensing shear (VanderPlas et al. 2012; Chang & Jain 2014; Szepietowski et al. 2014; Becker et al. 2016; Chang et al. 2018; Friedrich et al. 2018; Troxel et al. 2018; Bradshaw 2019), for the development and systematics testing of various galaxy and cluster cross correlations (Bleem et al. 2012; High et al. 2012; Pandey et al. 2019; Shin et al. 2019) and other statistics of the galaxy and lensing spatial distribution (Gruen et al. 2018; Friedrich et al. 2018), and for early preparation and testing of the science prospects of the DES (Gill et al. 2009; Davies et al. 2013; Chang et al. 2015; Asorey et al. 2016; Park et al. 2016), the WFIRST survey (Martens et al. 2019; Massara et al. 2021), and the LSST survey (Mao et al. 2018) as well as spectroscopic surveys (Saunders et al. 2014; Nord et al. 2016).

In DeRose et al. (2019a), we described the use of ADDGALS to create a suite of synthetic catalogs for the DES, extending the work described here to higher redshift while including a number of additional observational effects and presenting tests of a number of additional observables, including those related to cosmic shear, photometric redshifts, high-redshift galaxy clustering and lensing, and photometric cluster finding. That suite of catalogs as well as earlier versions were used extensively in the analysis of DES Science Verification and Y1 data (Clampitt et al. 2017; Krause et al. 2017; Sánchez et al. 2017; Abbott et al. 2018; Cawthon et al. 2018; Chang et al. 2018; Davis et al. 2018; Gatti et al. 2022; Gruen et al. 2018; MacCrann et al. 2018; Varga et al. 2019; Abbott et al. 2020). Catalogs produced using ADDGALS have continued to be used to facilitate DES Y3 cosmology analyses (Buchs et al. 2019; Cawthon et al. 2020; Gatti et al. 2020; Myles et al. 2021), and a description of the catalogs used for that work is given in DeRose et al. (2021b).

This paper proceeds as follows. In Section 2, we describe the simulations used in this work. In Section 3 our method of populating simulations with galaxies in a single-band rest-frame absolute magnitude is described. Tests of this part of the algorithm are presented in Section 4. In Section 5, we outline our method for assigning SEDs to simulated galaxies. The

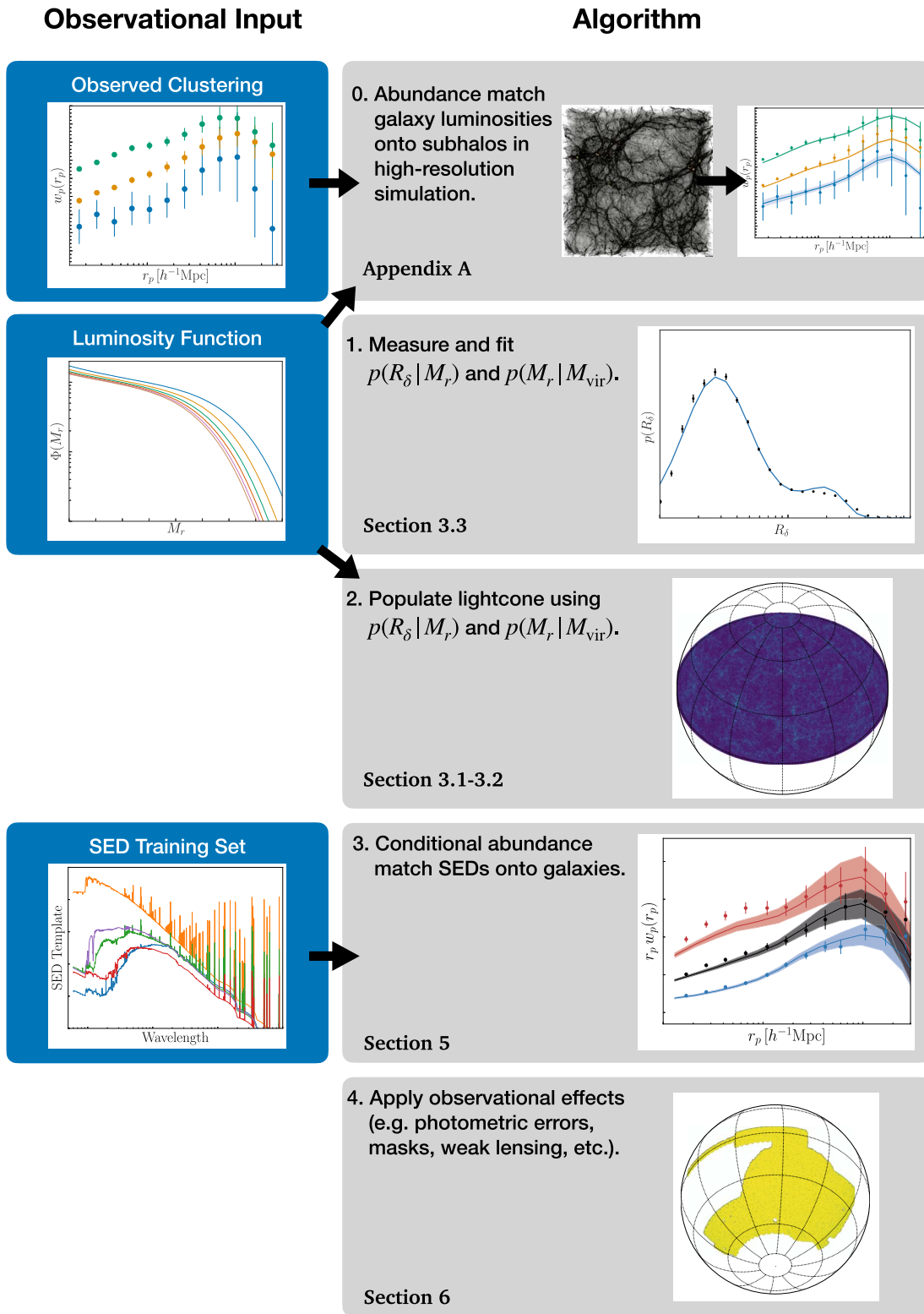


Figure 1. Flowchart of the ADDGALS algorithm. Observational inputs are listed in the left-hand column. In the first step, we use observed clustering and luminosity functions to constrain an SHAM model, applied to a simulation with resolved substructures (Appendix C). In the second step, we measure and fit a model for central galaxies given halo mass (Section 3.1) and for the dark matter density R_δ given luminosity for all other galaxies (Section 3.3). In the third step, we populate a lightcone using this algorithm. In the fourth step, we use an observed galaxy sample with luminosities, and SED properties to conditional abundance match SEDs onto simulated galaxies (Section 5). Finally, we apply observational effects (Section 6).

method that we employ to apply photometric errors to our simulations is described in Section 6. Tests of this method are presented in Section 7. In Section 8 we discuss the resolution requirements for ADDGALS. Finally, we conclude in Section 9

with a discussion of the strengths and limitations of the algorithm and future directions of research. Throughout this manuscript, we quote magnitudes using the AB system and $h = 1.0$ units.

Table 1
Description of Simulations Used for Training and Lightcone Construction

Name	z_{\min}	z_{\max}	L_{box}	N_{part}	m_{part}	$\epsilon_{\text{Plummer}}$	M_{\min}
T1	training only	training only	$400 h^{-1}\text{Mpc}$	2048^3	$4.8 \times 10^8 h^{-1}M_{\odot}$	$5.5 h^{-1}\text{kpc}$...
C250	resolution test only	resolution test only	$250 h^{-1}\text{Mpc}$	2560^3	$2.45 \times 10^8 h^{-1}M_{\odot}$	$0.8 h^{-1}\text{kpc}$...
L1	0.0	0.32	$1.05 h^{-1}\text{Gpc}$	1400^3	$3.3 \times 10^{10} h^{-1}M_{\odot}$	$20 h^{-1}\text{kpc}$	$6 \times 10^{12} h^{-1}M_{\odot}$
L2	0.32	0.84	$2.6 h^{-1}\text{Gpc}$	2048^3	$1.6 \times 10^{11} h^{-1}M_{\odot}$	$35 h^{-1}\text{kpc}$	$6 \times 10^{12} h^{-1}M_{\odot}$
L3	0.84	2.35	$4.0 h^{-1}\text{Gpc}$	2048^3	$5.9 \times 10^{11} h^{-1}M_{\odot}$	$53 h^{-1}\text{kpc}$	$10^{13} h^{-1}M_{\odot}$

Note. In this work, L2 is mainly used for resolution tests, and L3 is only used for high-redshift lightcone construction. Columns describe the simulation name, the minimum and maximum redshifts spanned by that simulation (z_{\min} and z_{\max}), although snapshots are saved at regular outputs between $z = 0 - 3$, the periodic box size used to generate the lightcones (L_{box}), the number of particles used in each simulation and the particle mass (N_{part} and m_{part}), as well as the force softening length ($\epsilon_{\text{Plummer}}$) and minimum halo mass that central galaxies are populated in (M_{\min}).

2. N-body Simulations

All simulations in this work were run using the code L-GADGET2 (Springel et al. 2005), a proprietary version of GADGET-2 optimized for memory efficiency and explicitly designed to run large-volume, dark matter-only N -body simulations. We have modified this code to create a particle lightcone output on the fly (see DeRose et al. 2019a, for details). The cosmology of these simulations is $(\Omega_{\text{m}}, \Omega_{\text{b}}, n_{\text{s}}, \sigma_8, H_0, w) = (0.286, 0.047, 0.96, 0.82, 70.0, -1)$. Initial conditions were generated with the second-order Lagrangian perturbation theory code 2LPTIC (Crocce et al. 2006) using linear power spectra computed with the CAMB code (Lewis 2004). Early versions of these simulations were generated on XSEDE supercomputers using the Apache Airavata⁸ workflow management framework (Erickson et al. 2012).

We use four N -body simulations with volumes of $(400 h^{-1}\text{Mpc})^3$, $(1.05 h^{-1}\text{Gpc})^3$, $(2.6 h^{-1}\text{Gpc})^3$, and $(4.0 h^{-1}\text{Gpc})^3$; the simulation parameters are summarized in Table 1. The first of these, deemed T1 (Training Simulation 1), requires sufficient resolution that an SHAM approach can reasonably model the galaxy distribution down to roughly $M_r = -19$ (see, e.g., Reddick et al. 2013; Lehmann et al. 2017). This simulation has $L_{\text{box}} = 400 h^{-1}\text{Mpc}$ and 2048^3 particles. At this resolution, the SHAM catalog is not strictly complete down to $M_r = -19$, as subhalos that would host galaxies with $M_r < -19$ near the cores of massive hosts become stripped and are no longer trackable by the halo finder, as they have too few particles (see Reddick et al. 2013 for a detailed discussion). However, comparisons with SDSS data show that the resolution is sufficient to model the observed two-point function within current observational constraints down to $M_r = -19$, except on the very smallest scales for the dimmest galaxies in this sample. It also does reasonably well for galaxies fainter than this limit (see DeRose et al. 2021a, for further discussion). The inability to accurately model small-scale clustering of the faintest samples is due in large part to subhalo disruption in T1 simulation. This is discussed at greater length in Section 8, where we compare with the C250 simulation, run with the same settings as the T1 simulation, but in a volume of $(250 h^{-1}\text{Mpc})^3$, using 2560^3 particles, and a force softening of $\epsilon = 0.8 h^{-1}\text{kpc}$. A lightcone output is not necessary for the T1 simulation, but merger trees are required to construct the abundance matching catalog. We save 100 simulation snapshots logarithmically spaced from $z = 12$ to

$z = 0$, which allows for the construction of accurate merger trees.

For the three larger simulations, L1, L2, and L3 (Lightcone Simulations 1–3), ten snapshots at redshifts

$$z = \{0.0, 0.10, 0.25, 0.4, 0.5, 0.7, 0.85, 1, 2, 3\}$$

are produced, as well as lightcones with areas of 10,313 square degrees each (one quadrant of the sky). The L1 simulation is used to produce the simulated galaxy catalog that we compare to SDSS in Section 7, while L2 and L3 are used solely for the resolution tests presented in Section 8 and for high-redshift lightcone construction, as described in DeRose et al. (2019a) and DeRose et al. (2021b). These simulations were run as part of the multiresolution ‘‘Chinchilla’’ Simulation suite; the higher-resolution simulations were first used in Mao et al. (2015) and Lehmann et al. (2017). When presented as ‘‘observed’’ catalogs, these simulations have been referred to as the ‘‘Buzzard’’ simulations.

2.1. Halo Finding

We identify halos with the publicly available adaptive phase-space halo finder ROCKSTAR⁹ (Behroozi et al. 2013b). ROCKSTAR is highly efficient, and has excellent accuracy (see, for example, the halo finder comparison in Knebe et al. 2011). It is particularly robust in galaxy mergers, important for the massive end of the halo mass function, and in tracking substructure, important for the abundance matching procedure applied to T1. We use M_{vir} strict spherical overdensity (SO) masses (Bryan & Norman 1998) here; additional halo mass definitions are output by ROCKSTAR using these halo centers. ROCKSTAR also outputs several other halo properties, including concentration, shape, and angular momentum (see Behroozi et al. 2013b, for details).

2.2. Merger Trees

For the highest-resolution T1 simulation, we track the formation of halos using 100 saved snapshots between $z = 12$ and $z = 0$, equally spaced in $\ln a$. The gravitationally consistent merger tree algorithm¹⁰ described in Behroozi et al. (2013c) is applied to construct halo merger trees. This algorithm explicitly checks for consistency in the gravitational evolution of dark matter halos between time steps, and leads to robust tracking. Details of the implementation and robustness tests can be found

⁸ <https://airavata.apache.org/>

⁹ <https://bitbucket.org/gfstanford/rockstar/>

¹⁰ <https://bitbucket.org/pbehroozi/consistent-trees>

in Behroozi et al. (2013c). Using the resulting merger trees, we are able to track the peak virial mass, M_{peak} , and velocity, v_{max} value for each identified subhalo.

2.3. Lagrangian Density Estimation

The final post-processing step for the dark matter simulations before we can run ADDGALS is to calculate the distance to the n th nearest particle for both identified halos and all simulation particles. ADDGALS uses the relation $P(R_\delta|M_r, z)$, where R_δ is the distance to n th nearest particle, and n is the number of particles whose mass sums to $M_\delta = 1.8 \times 10^{13} h^{-1} M_\odot$. We measure this Lagrangian density, R_δ , for every particle and halo in the each of the simulations presented in this work.

3. Connecting Galaxies to the Matter Distribution

We start by describing the first part of the ADDGALS algorithm, which populates a dark-matter-only simulation with galaxies using a model trained on a higher-resolution simulated galaxy catalog. The algorithm is designed to work on the matter distribution from either a simulation snapshot or lightcone output. A key strength of the algorithm is its ability to use relatively low-resolution dark matter simulations. Consequently, we operate directly on the dark matter particle distribution, using the density information described in Section 2.3 to assign galaxy properties. The algorithm is designed to insert galaxies with single-band absolute magnitudes. While this quantity could be chosen to be anything that is reasonably well correlated with density, in the present work, we use the SDSS r -band magnitude k -corrected to $z=0.1$, $M_r^{0.1}$, hereafter M_r .

Here we train ADDGALS to reproduce the galaxy–dark matter connection in an abundance matching (SHAM) model. We use the best-fit model from Lehmann et al. (2017) to assign galaxies to dark matter halos. This procedure, including the luminosity function and implementation details, are described in Section A. In principle, the same type of mapping can be tuned to other catalogs, such as those constructed with SAMs, hydrodynamical simulations, or other empirical models. ADDGALS is able to approximate catalogs produced by the SHAM model because local density measurements contain information about halo mass and halo-centric distance, allowing for the accurate reproduction of the HOD and radial profiles of the catalog that ADDGALS is tuned to. Limitations of the SHAM catalog that ADDGALS is tuned to, such as the effects of artificial subhalo disruption on the satellite populations of massive halos, are also inherited.

Broadly, this part of the ADDGALS algorithm proceeds in two steps, described in the following subsections:

1. Central galaxies are placed on all resolved host halos above the some minimum halo mass threshold, M_{min} , as listed in Table 1 (Section 3.1).
2. The one-dimensional PDF of local dark matter density around galaxies conditioned on absolute magnitude measured from the SHAM model is used to assign the rest of the galaxies (Section 3.2).

3.1. Populating Resolved Central Galaxies

A statistical relationship between halo mass and its primary galaxy’s absolute magnitude, $p(M_{r,\text{cen}}|M_{\text{vir}})$, is assumed in order to populate central galaxies. The mean of this distribution

is given by

$$\langle M_{r,\text{cen}} \rangle (M_{\text{vir}}) = M_{r,0} - 2.5[a \log x - (1/k) \log(1 + x^{bk})], \quad (1)$$

where $x = M_{\text{vir}}/M_c$ and a , b , k , M_c , and $M_{r,0}$ are redshift-dependent fitting parameters. This form was proposed by Vale & Ostriker (2006) to match early SHAM catalogs and has been shown to provide a good fit to observational catalogs (Zheng et al. 2007; Hansen et al. 2009). A Gaussian scatter in absolute magnitude at fixed mass is assumed such that a halo with mass M_{vir} is assigned a magnitude drawn from

$$p(M_{r,\text{cen}}|M_{\text{vir}}) = \mathcal{N}(\langle M_{r,\text{cen}} \rangle (M_{\text{vir}}), \sigma_{M_{r,\text{cen}}}) \quad (2)$$

where $\sigma_{M_{r,\text{cen}}} = 0.425$, matching the scatter assumed in the SHAM model. Tests have shown that this relation must be applied at least for all host halos more massive than $M_{\text{vir}} \sim 10^{13} h^{-1} M_\odot$ to accurately reproduce the projected clustering of luminosity-selected galaxies (see Section 8 for further discussion of resolution requirements).

Equation (1) is then fit to the SHAM catalog, constructed from the T1 simulation, in each time snapshot over the mass range $10^{12} h^{-1} M_\odot \leq M_{\text{vir}} < 10^{15} h^{-1} M_\odot$. When populating lightcone simulations, the fit from the snapshot that is closest to the redshift under consideration is used. Evolution in this relation over the redshift ranges between snapshots is negligible. Validation of this relation is described in Appendix D. Once $p(M_{r,\text{cen}}|M_{\text{vir}})$ has been determined, it is used to populate all central galaxies down to the halo mass limits in Table 1 by sampling from the distribution in Equation (2), conditioned on the mass of each host halo in the simulation. We note that the resolution of L1 would enable us to go to lower masses, but this is not required to match the clustering properties of the higher-resolution simulation (Section 8), so we keep this limit constant between L1 and L2 for continuity.

3.2. Populating Galaxies in Unresolved Structures

The resolution of the lightcone simulations used here is such that central galaxies assigned using the method described above constitute only a small fraction of all galaxies that would be observed by deep photometric surveys. To populate the rest of the galaxies, the relationship between large-scale dark matter density and galaxy rest-frame magnitude, $p(R_\delta|M_r, z)$, is used. R_δ is defined as the radius enclosing a mass scale of $M = 1.8 \times 10^{13} h^{-1} M_\odot$, characterizing the local dark matter density around galaxies. For the L1 simulation, this radius corresponds to the distance to the 538th nearest dark matter particle. Section 3.3 describes how this relation is determined from an SHAM catalog. This mass scale is roughly equivalent to M_* , the typical collapsing halo mass, at $z=0$ for this cosmology, and thus effectively distinguishes between halos of different biases.

In order to parallelize the ADDGALS algorithm, we divide the lightcone simulations into domains of approximately $(200 h^{-1} \text{Mpc})^3$ in volume. This is accomplished by dividing the sky in angle as well as redshift. In a given patch with a redshift range of $z_{\text{low}} < z < z_{\text{high}}$, we create a catalog of galaxies with magnitudes and redshifts $\{M_{r,i}, z_i\}$, where $i = 1, \dots, N$, and

N is the total number of galaxies, given by:

$$N = \int_{z_{\text{low}}}^{z_{\text{high}}} dz \frac{dV}{dz} \int_{-\infty}^{M_{r,\text{min}}(z)} \phi_{\text{unres}}(M_r, z), \quad (3)$$

where $M_{r,\text{min}}$ is the faintest absolute magnitude that we populate galaxies to, typically chosen to yield a catalog complete to a particular observed r -band magnitude limit, and ϕ_{unres} is the luminosity function of all objects to be placed on unresolved structures in the simulation. This function subtracts central galaxies from the total luminosity function (which is fit to SDSS as described in Section A) in order to avoid double-populating bright galaxies, and thus is specified by

$$\begin{aligned} \phi_{\text{unres}}(M_r, z) &= \phi(M_r, z) - \phi_{\text{res}}(M_r, z) \\ &= \phi(M_r, z) \\ &\quad - \int_{M_{\text{min}}}^{\infty} dM_{\text{vir}} p(M_{r,\text{cen}}|M_{\text{vir}}, z) n(M_{\text{vir}}, z), \end{aligned} \quad (4)$$

where $n(M_{\text{vir}}, z)$ is the halo mass function in the simulations. We modulate the normalization of the luminosity function by the local dark matter overdensity,

$$\phi_{i,\text{local}} = \phi_i(1 + \delta). \quad (5)$$

Here $\phi_{i,\text{local}}$ is the normalization of the luminosity function in the local domain i , and δ is the matter overdensity within the domain. This avoids fixing the number density of galaxies on the scale of the domain size, but can induce a scale-dependent bias on scales of similar size to the domains. We can see the reason for this as follows. Note that $b(r) = \delta_g/\delta_m$, where the overdensities are smoothed on a radius r . Equation (5) enforces $\delta_g(r > r_{\text{domain}}) = \delta_m(r_{\text{domain}})$, where $\delta_m(r_{\text{domain}})$ is the matter overdensity on the scale of the domain size. Thus, $b(r > r_{\text{domain}}) = \delta_m(r_{\text{domain}})/\delta_m(r)$, and is scale dependent for $r > r_{\text{domain}}$. The domains are taken to be at least $(200h^{-1}\text{Mpc})^3$, and thus the effect of this choice is negligible for most applications. However, this choice may have an impact on covariance matrices involving scales larger than the domain size, which requires further investigation. The size of these domains is chosen as a compromise between this effect and the run time of the algorithm, as ADDGALS can be run in parallel over each domain.

Redshifts of each galaxy, z_i , are then drawn from

$$P(z) = \frac{1}{N} \frac{dV}{dz} \int_{-\infty}^{M_{r,\text{min}}} dM_r \phi_{\text{unres}}(M_r, z), \quad (6)$$

and magnitudes, $M_{r,i}$, are drawn from $\phi_{\text{unres}}(M_r, z_i)$. With magnitudes and redshifts assigned to every galaxy, densities $\{R_{\delta,i}\}$ are drawn from $p(R_{\delta}|M_{r,i}, z_i)$, and each galaxy is then assigned to a particle, going from brightest to faintest, with the closest match in redshift and density that has not already been assigned. The details of this process are described in Appendix C.

At this point, the described algorithm produces a catalog of galaxies with r -band absolute magnitudes. This algorithm is a very efficient way to generate a large-volume synthetic catalog with faint galaxies using primarily simulations with modest resolution. Additionally, as long as abundance matching in the r band works well at high redshifts, we expect that the galaxy distribution should match the clustering at a wide range of redshifts. Note that the same algorithm can also be used to populate co-moving snapshots by fixing z in the above

equations to the redshift of the snapshot output. The next section describes how $p(R_{\delta}|M_{r,i}, z_i)$ is determined from an SHAM catalog on a high-resolution simulation.

As we show in Section 4 and Appendix D, with this algorithm we can create a galaxy catalog that matches the projected galaxy two-point function, HOD, conditional luminosity function, and galaxy profiles in halos of a galaxy catalog populated using SHAM in a higher-resolution simulation.

3.3. Determining the $p(R_{\delta}|M_r, z)$ Relation

The form of $p(R_{\delta}|M_r, z)$ is the crux of the ADDGALS algorithm. We have found the following bimodal form is a good fit to our simulations:

$$\begin{aligned} p(R_{\delta}|M_r < x, z) &= p(R_{\delta}; \Theta(x, z)) \\ &= (1 - p) e^{-(\ln(R_{\delta}) - \mu_c)^2 / 2\sigma_c^2} / R_{\delta} \sqrt{2\pi} \sigma_c \\ &\quad + p e^{(R_{\delta} - \mu_f)^2 / 2\sigma_f^2} / \sqrt{2\pi} \sigma_f. \end{aligned} \quad (7)$$

This gives the probability that a galaxy with magnitude $M_r < x$ at redshift z has a local dark matter density, R_{δ} . Each of this relation's five free parameters, $\Theta(x, z) = \{\mu_c, \sigma_c, \mu_f, \sigma_f, p\}$, are functions of galaxy absolute magnitude and redshift, and the dependence of $\Theta(x, z)$ on these variables is modeled using a Gaussian process as described in Appendix B.

Figure 2 shows the distribution of $p(R_{\delta})$ for bins in galaxy magnitude and redshift (left) and galaxy magnitude and host halo mass (right). The full distribution $p(R_{\delta}|M_r < x, z)$ in bins of magnitude and redshift in the input SHAM model (points) is well reproduced by the ADDGALS model applied to the T1 simulation (blue line). The reduced chi-squared values for these fits can be large, $O(10 - 100)$, but the median absolute deviation is less than 2.5% for all redshift and magnitude bins.

The orange and green lines in this figure show the same distributions for central and satellite galaxies in the SHAM, to indicate which region of this distribution they populate. At low luminosity (bottom rows), these two populations are easily separated by density. At higher luminosity (top row), the two populations cannot be distinguished by density; this motivates separate modeling of bright central galaxies through $\langle M_{r,\text{cen}} \rangle(M_{\text{vir}})$ so that central galaxies can be distinguished from bright satellites in massive systems.

The right side of Figure 2 shows the distribution of $p(R_{\delta})$ in bins of halo mass and galaxy magnitude at redshift $z=0$, $p(R_{\delta}|M_{\text{vir}}, M_r < x, z=0)$. Splitting the distribution in this way gives intuition for how assigning galaxies by R_{δ} can approximate assignment by halo mass, even in simulations that are lower resolution than the relevant resolved halos. At high mass (right column), we see that this distribution is highly peaked toward small R_{δ} (high densities), and satellites and centrals are easily separated in R_{δ} space. The movement of this peak with mass is what enables assignment by R_{δ} to distinguish between different halo masses. The smoothing scale used here, $(1.8 \times 10^{13} h^{-1} M_{\odot})$, effectively distinguishes more biased halos above the smoothing scale from lower-mass halos below the smoothing scale (left most column), where halo bias is relatively flat. For halos below the mass smoothing scale, the distribution $p(R_{\delta}|M_{\text{vir}}, M_r < x, z)$ broadens, and there is much more scatter in M_{vir} when assigning by R_{δ} . Due to this broadening, the ADDGALS algorithm is susceptible to scattering galaxies between different halo masses at fixed R_{δ} . This can lead to Eddington-like biases in HODs in ADDGALS, where

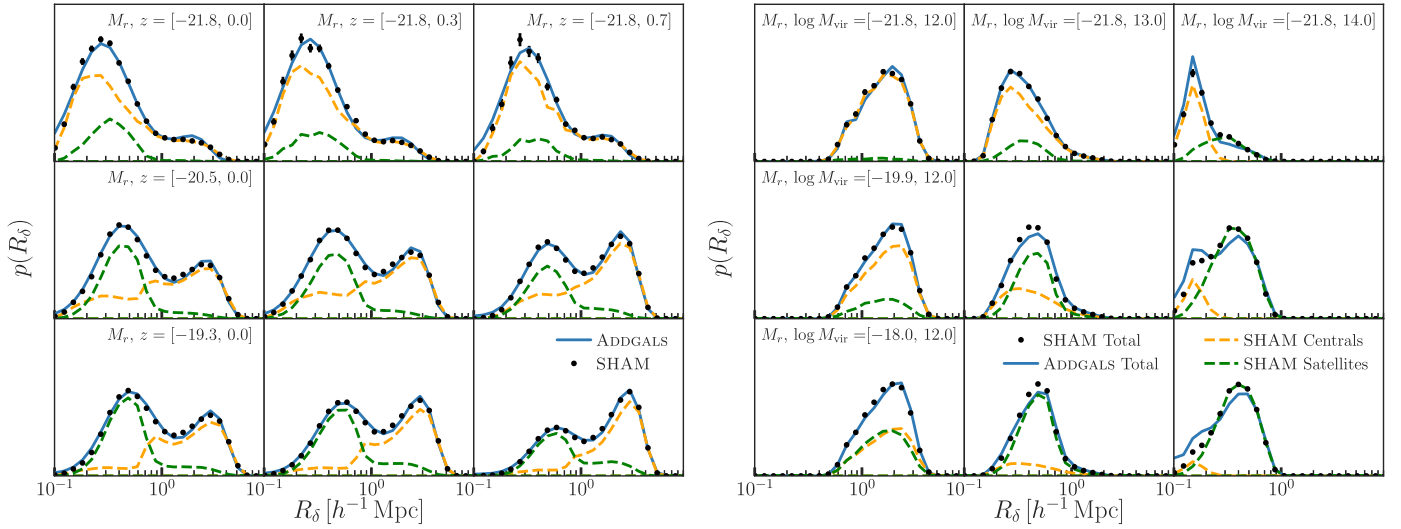


Figure 2. PDF of dark matter densities, characterized by R_δ , the radius enclosing a mass of $1.8 \times 10^{13} h^{-1} M_\odot$, for various galaxy populations in the simulations. Both panels compare the ADDGALS distribution (blue lines) to the SHAM distribution (black points) in the T1 simulation. Dashed green and orange lines represent the R_δ distributions for satellite and central galaxies, respectively, in the SHAM catalog. The left panel compares the R_δ distributions for galaxies, binned by absolute magnitude (rows), residing in all halo masses at different redshifts (columns). Fainter central galaxies tend to live in less massive halos, corresponding to large R_δ , while satellites are hosted by more massive halos corresponding to small R_δ , leading to the observed bimodality in $p(R_\delta)$. The right panel compares the R_δ distributions at $z = 0$ for galaxies as a function of absolute magnitude (rows) and host halo mass (columns). The agreement shows that ADDGALS is able to successfully reproduce the density distribution of the SHAM model.

galaxies that should be placed in halos with masses less than the smoothing mass scatter up into halos with masses approximately at the smoothing mass. However, in this regime, halo bias is relatively flat so this scatter does not significantly impact the projected clustering signals in ADDGALS.

3.4. Algorithm Overview

The algorithm steps can be summarized as follows:

1. High-resolution modeling: apply an SHAM model to high-resolution N -body snapshots.
2. High-resolution training:
 - (a) calibrate the luminosity–density–redshift relation, $p(R_\delta | M_r, z)$ from the SHAM model;
 - (b) calibrate the central luminosity–halo mass relation, $p(M_{r,\text{cen}} | M_{\text{vir}})$ from the SHAM model.
3. Populating lightcone simulations:
 - (a) populate central galaxies based on $p(M_{r,\text{cen}} | M_{\text{vir}})$;
 - (b) populate the rest of the galaxies based on $p(R_\delta | M_r, z)$ and the luminosity function.

The final result is a synthetic galaxy catalog containing positions, velocities, and single-band photometric information. Next we validate the steps above using observations from the SDSS.

4. Validation of the Luminosity–Density Assignment

Here, we present a number of tests validating the ability of ADDGALS to reproduce the properties of the T1 SHAM model in the lower-resolution L1 simulation. The tests in this section compare an ADDGALS catalog run on the $z = 0$ snapshot output of the L1 and L2 simulations and an SHAM catalog run on the $z = 0$ snapshot output of the T1 simulation unless otherwise noted.

The left side of Figure 3 compares the projected correlation function of the T1 ADDGALS, L1 ADDGALS, and L2 ADDGALS catalogs with the T1 SHAM catalog and the SDSS measurements

presented in Reddick et al. (2013). The function $w_p(r_p, \pi)$ is measured in the snapshots using the Landy–Szalay (Landy & Szalay 1993) estimator, i.e., $w_p(r_p, \pi) = (DD - 2DR + RR)/RR$, placing the observer at infinity and assuming periodic boundary conditions, using 13 logarithmically spaced bins in r_p between $0.1 h^{-1} \text{Mpc}$ and $40 h^{-1} \text{Mpc}$, subsequently integrating these measurements along the line of sight out to $\pi_{\text{max}} = 60 h^{-1} \text{Mpc}$ to obtain $w_p(r_p)$. Ten times as many random points as galaxies are used to estimate DR and RR , where the randoms are distributed uniformly in each sub-volume. Errors are estimated via jackknife using 64 sub-volumes for each simulation.

We use the best-fit SHAM model from Lehmann et al. (2017), and as such, the agreement between the SHAM catalog and SDSS is good, albeit with relatively large errors on the SHAM measurements for the brighter samples. Details of how the SHAM catalog are constructed are described in Section A. The ADDGALS catalog and the SHAM catalog are consistent with each other at most scales and magnitudes. Discrepancies between the ADDGALS catalogs and the SDSS data can be seen in the $M_r < -22$ and $M_r < -19$ measurements. Given the large errors on the SHAM catalog for the $M_r < -22$ magnitude cut, it is unclear whether this discrepancy is due to a disagreement between ADDGALS and the SHAM model, or whether ADDGALS and the SHAM model agree well, and the SHAM model disagrees with the data. Lehmann et al. (2017) found a marginal preference for lower scatter at brighter luminosities, which is consistent with the latter of these two possibilities. We also make use of a slightly different luminosity function than Lehmann et al. (2017), with the main difference coming at the brightest end, where our luminosity has a shallower slope. This may also lead to a reduced clustering amplitude in the $M_r < -22$ bin.

For $M_r < -19$, the ADDGALS and SHAM catalogs are in good statistical agreement for $r_p > 1 h^{-1} \text{Mpc}$, but deviate significantly from SDSS at scales $r_p < 1 h^{-1} \text{Mpc}$. The SHAM model suffers from artificial subhalo disruption in this regime, leading

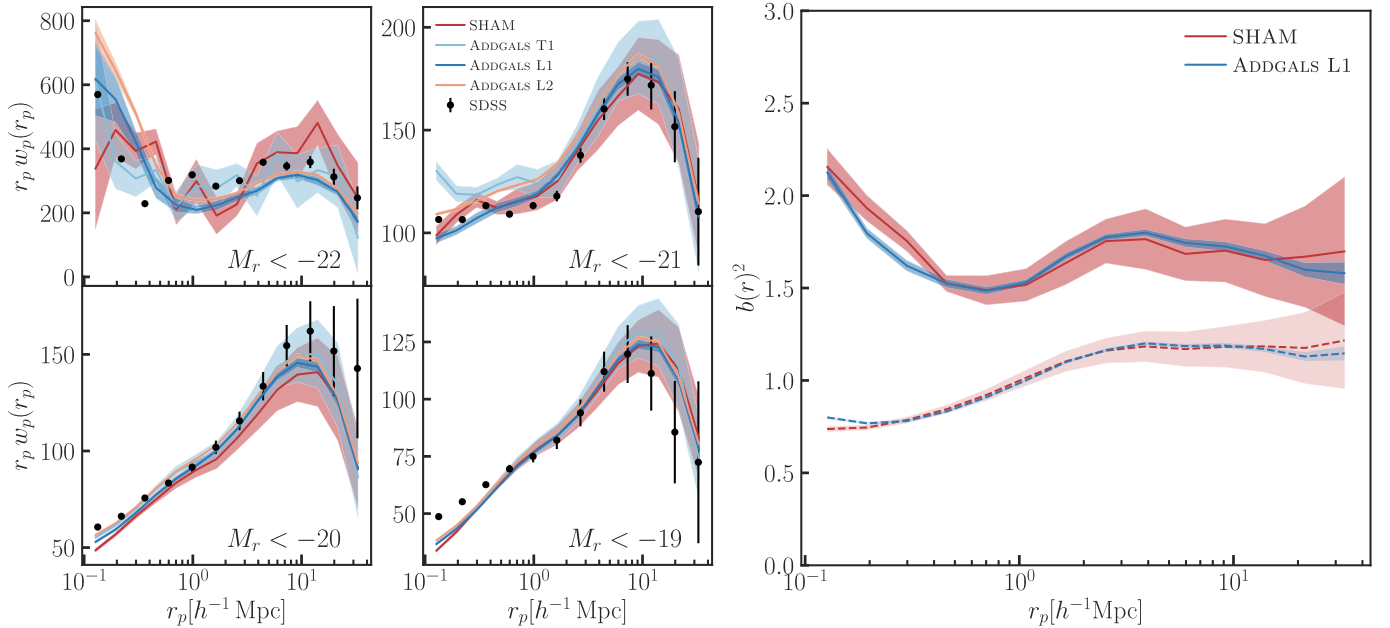


Figure 3. Comparison of ADDGALS clustering and bias with that measured in the SHAM model it is tuned to. Left: projected correlation functions for an SHAM model applied to the $z = 0$ snapshot of the T1 simulation, and ADDGALS models trained on that SHAM run on the $z = 0$ snapshots of the T1, L1, and L2 simulations. The shaded regions and error bars are the 1σ errors, estimated via a jackknife procedure described in the text. Each panel shows a different magnitude threshold. The corresponding SDSS measurements from Reddick et al. (2013) are shown for comparison. Agreement between ADDGALS catalogs based on different resolution simulations and the SHAM model are generally good. Discrepancies between the small-scale simulation measurements and data are discussed in Section 4. Right: bias as a function of scale for the L1 ADDGALS catalogs and the SHAM model it is tuned to, indicating good agreement. The solid lines are for all galaxies with $M_r < -21$, and the dashed lines are $M_r < -19$.

to lower small-scale clustering, and the ADDGALS model has inherited this issue through the $p(R_\delta|M_r, z)$ distribution. Differences between the ADDGALS catalogs due to differences in simulation resolution are discussed in Section 8.

The right-hand side of Figure 3 compares the behavior of galaxy bias between the ADDGALS and SHAM catalogs. The bias measurements are made by taking the ratio of $w_p(r_p)$ for galaxies and that measured on the matter distribution in each respective simulation. Given the agreement between the projected correlation functions of the SHAM model and ADDGALS, the agreement seen here is expected. A notable feature in this figure is the scale at which the different samples conform to a linear bias model, i.e., $\delta_g(r) = b_1 \delta_m(r)$, on large scales. For the fainter $M_r < -19$ sample, galaxy bias becomes linear in both catalogs for scales with $r_p > 4h^{-1}\text{Mpc}$. For the brighter $M_r < -21$ sample, the SHAM catalog also appears to behave linearly for $r_p > 4h^{-1}\text{Mpc}$. The ADDGALS measurements are fully consistent with the noisier SHAM measurements, but the smaller error bars in these measurements show hints of nonlinear bias out to slightly larger scales. This result is expected for this more massive galaxy sample.

We compare the radial profiles of galaxies around host halos between the ADDGALS and SHAM catalogs in Figure 4. The measurements from ADDGALS that are run on the T1 (light blue), L1 (dark blue), and L2 (orange) simulations are included. All curves are normalized so that the SHAM radial profile equals one on the largest scale in the figure. We indicate where we expect resolution effects in the matter density profiles of the host halos by plotting curves below this scale with a dashed line. This scale is approximated by five times the force softening scale used in each simulation.

We see that these radial profile measurements exhibit significant differences between ADDGALS and SHAM.

Above $\sim 200 h^{-1}\text{kpc}$, the two models agree well, as expected by the agreement between projected correlation functions for the two models. Below this scale, in both mass bins shown here, the SHAM catalog experiences a flattening, and becomes inconsistent with the expectation of profiles with Navarro–Frenk–White (NFW) functional forms shown by the black line (Navarro et al. 1996). The NFW prediction shown here assumes the mean host mass in the bin, the mass–concentration relation from Diemer & Joyce (2019), and is normalized so that it matches the SHAM curves at R_{vir} . The reason for this deviation from an NFW expectation for SHAM is likely artificial subhalo disruption for halos that have close pericentric passages (van den Bosch et al. 2018; van den Bosch & Ogiya 2018).

We can understand the behavior of the ADDGALS measurements in the following way. Under the assumptions of the ADDGALS algorithm, it is possible to write the radial profile of galaxies of absolute magnitude M_r in a halo of mass M_h as

$$\rho(r|M_r, M_h) \propto \int p(r|R_\delta, M_h) p(R_\delta|M_r) dR_\delta \quad (8)$$

$$= \int \frac{p(r|M_h) p(R_\delta|r, M_h)}{p(R_\delta|M_h)} p(R_\delta|M_r) dR_\delta. \quad (9)$$

$p(r|R_\delta, M_h)$ is the PDF of matter particle distances to centers of halos of mass M_h , given that the particle has a local density measurement of R_δ . The first line above follows from the fact that ADDGALS assigns a galaxy with absolute magnitude M_r to a random particle with density R_δ , where R_δ is a random draw from $p(R_\delta|M_r)$. The second line above is obtained from the first via application of Bayes theorem.

We see that we can express ADDGALS radial profiles in terms of $p(R_\delta|M_r)$, the normalized radial profile of matter in halos of

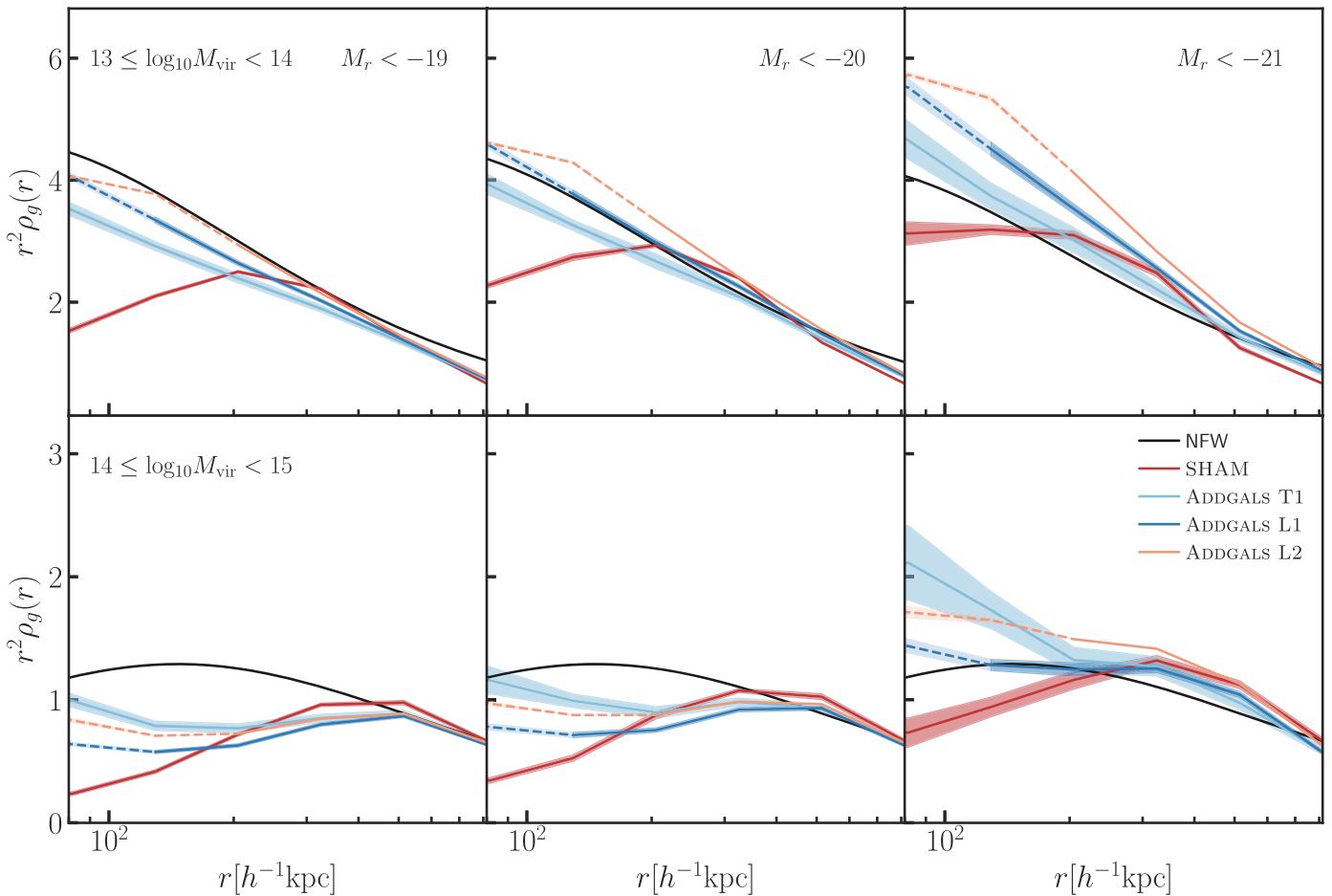


Figure 4. Radial profiles of galaxies in group- and cluster-sized halos for SHAM, ADDGALS T1, ADDGALS L1, and ADDGALS L2 catalogs. Columns show different absolute magnitude cuts given by the labels in each panel, and rows show different halo mass bins. Each panel is normalized to the SHAM curves on the largest scale plotted; uncertainties for each measurement are estimated using jackknife. The lines transition from solid to dashed at five times the force softening length of each respective simulation in order to approximate the scale where we expect resolution to affect the matter profiles of these halos. The black line indicates a Navarro–Frenk–White (NFW) profile for the mean halo mass in the bin, using the Diemer & Joyce (2019) mass–concentration model and normalized to match the SHAM profiles at R_{vir} . Agreement between the catalogs is generally good at scales larger than $200h^{-1}\text{kpc}$, which approximately corresponds to the scale imposed by the mass used to calculate R_δ . This scale is relatively independent of halo mass, modulo changes in the mean halo concentration as a function of halo mass. Below this scale, R_δ becomes approximately constant, and the SHAM and ADDGALS profiles no longer track each other. At scales less than this smoothing scale in the less massive bin, the ADDGALS profiles approximate NFW profiles much more closely than the SHAM catalog, which is affected by artificial subhalo disruption on these scales. On the smallest scales depicted here, the L2 ADDGALS profiles begin to deviate near the resolution limits of the simulation, with the slope of the profiles turning over in a characteristic manner. In the more massive bin, none of the catalogs are well described by an NFW profile. At these masses, the ADDGALS smoothing scale can probe smaller fractions of the halo virial radius, and subhalo disruption effects that become important for satellite galaxies in the SHAM are inherited by $p(R_\delta|M_r)$, and thus the ADDGALS catalogs. This causes deviations from NFW profiles for all catalogs above the ADDGALS smoothing scale. For a more quantitative discussion, see Section 4.

mass M_h , $p(r|M_h)$, the distribution of R_δ as a function of halo-centric radius, r , $p(R_\delta|r, M_h)$, and $p(R_\delta|M_h)$. Note that in the limit where $p(R_\delta|r, M_h)$ is constant as a function of r , then $\rho(r|M_r, M_h) \propto p(r|M_h)$. This is the case on small scales ($\lesssim 200h^{-1}\text{kpc}$), where M^* , the mass scale used to calculate R_δ , is significantly larger than the mass enclosed within radius r . This makes it clear that the flattening of the slope in the ADDGALS L2 catalog on small scales (and for L1 on scales smaller than those plotted here) in the lower-mass bin of Figure 4 is due to a flattening in the actual matter profiles in halos at those scales, which is close to five times the force softening radii used in these simulations where such a turn over is expected (DeRose et al. 2019b). When using a higher-resolution simulation like T1, this flattening is no longer seen.

For the lower-mass bin, this implicit smoothing scale is approximately the same size as R_{vir} , and so the ADDGALS profiles approximate an NFW profile well for the entire

one-halo term. For the higher-mass bin, the smoothing scale is significantly less than R_{vir} and so the one-halo term exhibits significantly more complicated behavior. Above the smoothing scale, the ADDGALS profiles track the SHAM catalog profiles well. At scales less than R_{vir} but greater than the smoothing scale, the SHAM catalog is significantly flattened by artificial subhalo disruption, and so on these scales, the ADDGALS catalog inherits the same flattened profile. On scales below the smoothing scale, the ADDGALS catalog reverts to being proportional to the matter profile, leading to the observed upturn relative to the SHAM catalog. This flattening of the ADDGALS profiles at high mass has significant implications for optical galaxy cluster finding, as it leads to a deficit of galaxy number densities in massive clusters with respect to that observed in data as discussed in Section 7.2. Additional validation of the ADDGALS catalogs is provided in Appendix D.

We note that a precise match between $P(R_\delta|M_r, z)$ in ADDGALS and SHAM is extremely important in achieving the level of agreement seen in the above comparisons. Even relatively small changes in this distribution make these matches appreciably worse. These comparisons demonstrate the real strength of the ADDGALS algorithm. Here, we are able to produce simulated galaxy catalogs that are complete in absolute magnitude and reproduce observed galaxy clustering properties using an N -body simulation that has a particle number density only a factor of ~ 100 higher than the galaxy density. Additionally, tests have shown that such an agreement is possible for simulations with significantly lower resolution, where the number densities differ by only as much as ~ 20 . The ability to create a realistic galaxy distribution on such modest-resolution simulations allows for the creation of very large-volume synthetic catalogs, appropriate for modeling large photometric and spectroscopic surveys such as SDSS, DES, and LSST, without resorting to any sort of replication techniques or highly expensive simulations, as would be required for most other algorithms.

5. Assignment of Galaxy SEDs

Once the galaxies have been populated with phase-space positions and r -band luminosities, we assign SEDs to each galaxy in the second part of the ADDGALS algorithm. While the SED assignment algorithm was developed in conjunction with the galaxy assignment method discussed above, the algorithm is independent and able to operate on any galaxy catalog that already has absolute magnitudes defined in one band. This part of the algorithm, which is referred to as ADDSEDS (Adding Density-Determined SEDs) when used on its own, has been used independently from the first step of ADDGALS in previous works, based on earlier versions of the present algorithm (see, e.g., Gerke et al. 2013; Mao et al. 2018).

ADDSEDS assumes that galaxy SEDs are set by both absolute magnitude and galaxy environment and uses a training set consisting of the SDSS DR7 VAGC (Blanton et al. 2005), whose SEDs are mapped onto the simulated galaxies. We cut the training set to $0.005 < z < 0.2$, since the bright, higher-redshift objects and very faint low-redshift objects represent a biased sample with respect to the rest of the population of galaxies. The final training set consists of approximately 600,000 spectroscopic galaxies from the SDSS main sample.

For each galaxy in the simulated galaxy catalog, the set of SDSS galaxies in a bin of M_r around each simulated galaxy is identified, and one SED is randomly chosen from this set and assigned to the simulated galaxy. The assumed bin width depends on M_r as $\Delta M_r = \Delta M_{r,0}(22.5 + M_r)$, where $\Delta M_{r,0} = 0.1$, and ΔM_r is never allowed to decrease below $M_{r,0}$. If no galaxy in SDSS is found, the bin width is relaxed to $\Delta M_r = \Delta M_{r,0}(22.5 + M_r)^2$; the latter criteria always enable a match to be found. These bin widths have been tuned in order to minimize discreteness effects in color space due to assigning the same SDSS SED repeatedly to many simulated galaxies.

After this initial step, an environmental dependence of the SED assignment is imparted on the catalog. This is accomplished by correlating the $z = 0.1$ frame $g - r$ color with a local density proxy that can be accurately measured in modest-resolution N -body simulations. The proxy that we have found to work well is the distance between the galaxy in question and the nearest halo above a mass threshold, $M_{h,\text{cut}}$. We refer to this proxy as R_h .

In detail, $g - r$ colors are mapped onto the simulated galaxies by enforcing the following ansatz:

$$P(<g - r|M_r) = P(<\widetilde{R}_h|M_r) \quad (10)$$

where \widetilde{R}_h is a noisy version of R_h , and the Pearson correlation coefficient between $\text{Rank}(R_h)$ and $\text{Rank}(\widetilde{R}_h)$ is set to r_{corr} . In doing so, we allow for an imperfect correlation between R_h and $g - r$, which is necessary to match observed clustering statistics as a function of $g - r$. In order to reduce discreteness effects, $P(<g - r|M_r)$ and $P(<\widetilde{R}_h|M_r)$ are computed in sliding windows around each galaxy, such that the width of the window in M_r yields 100 galaxies with which to estimate the above distributions. The values for $M_{h,\text{cut}}$ and r_{corr} are free parameters of the model, tuned to reproduce color-dependent clustering in SDSS. This work uses the best-fit values of these parameters from DeRose et al. (2021a), where additional implementation details for this model can be found.

This is very similar in spirit to conditional abundance matching (CAM) models that first assign magnitudes to halos via abundance matching, and then assign colors to galaxies at fixed magnitude by making the ansatz that $\text{Rank}(X_h) \sim \text{Rank}(g - r)$, where X_h is usually taken to be a dark matter halo property such as formation time or accretion rate (Masaki et al. 2013; Hearin et al. 2014; Watson et al. 2015).

Once a $g - r$ value from SDSS is assigned to each galaxy, the SED associated with that $g - r$ value is mapped onto the simulated galaxy as well. The galaxy SEDs are represented as five SED template coefficients, α_i , using the templates determined to be used in the KCORRECT algorithm (Blanton et al. 2003a) as the basis. Since some tolerance in M_r is allowed in the match between simulated and data galaxies, the SED obtained from the data must be normalized such that it gives the absolute magnitude originally assigned to the simulated galaxy. This is accomplished by re-normalizing the KCORRECT coefficients such that

$$-2.5 \log_{10} \frac{\alpha'_i}{\alpha_i} = M_{r,\text{sim}} - M_{r,\text{train}} \quad (11)$$

where α'_i are the re-normalized coefficients, $M_{r,\text{sim}}$ is the r -band absolute magnitude assigned to the simulated galaxy, and $M_{r,\text{train}}$ is the absolute magnitude of the matched training set galaxy. Using these coefficients, the SEDs can be integrated over filter bandpasses in order to produce observed galaxy magnitudes.

Here we emphasize a few key points of the algorithm. First, we note that the training set SEDs are mapped to synthetic galaxies without using redshift information. When combined with the magnitude limit of our training set, this means that the number of galaxies in the training set varies strongly as a function of M_r , with the highest density at $M_r \sim -20$. Additionally, no galaxy evolution models are applied. In particular, the only two ways in which we account for redshift evolution of colors are via evolution of galaxy magnitudes *before* the SED is selected (which generally brightens galaxies with redshift), and via redshifting of the SED to determine the observed galaxy magnitudes. We also apply a redshift- and luminosity-dependent evolution of the red fraction of galaxies as described in Appendix E.2 of DeRose et al. (2019a); although, this is not important for the SDSS comparisons

presented here. We assume both that the typical rest-frame colors of galaxies are unchanged and that the color–environment–luminosity relation remains unchanged as a function of redshift. Both of these assumptions are certainly incorrect in detail. Given these limitations, the photometry that is produced at high redshift should be treated with caution. Future development will address these issues. Nonetheless, these corrections work extremely well in reproducing galaxy properties over the redshift range of SDSS. In a companion paper extending this algorithm to higher redshifts in the context of DES (DeRose et al. 2019a), we addressed one aspect of galaxy evolution by adjusting the relative fraction of red and blue galaxies (note that this was applied to a slightly older version of ADDSEDS).

5.1. Summary of SED Assignment Algorithm

We briefly summarize the most important steps in our SED assignment algorithm:

1. Compile a training set of spectroscopic galaxies.
2. Calculate the distance to the nearest massive halo, R_h , for each simulated galaxy.
3. Conditional abundance match $g - r$ colors in the training set to \tilde{R}_h , a noisy version of R_h .
4. Use the CAM relationship to map SEDs from the training set galaxy to the synthetic galaxy.
5. Redshift the SED and convolve with filter pass bands to determine observed magnitudes.

Applying this algorithm results in a synthetic photometric catalog down to some limiting absolute magnitude. Note that when attempting to model a magnitude-limited survey, such as SDSS, it is necessary to generate synthetic galaxies to some limiting absolute magnitude, $M_{r,\text{lim}}(z)$, as a function of redshift. Because of the significant scatter in the $M_r - m_r(z)$ relation due to variation in galaxy SEDs, it is generally necessary to create significantly more galaxies than necessary, cutting the catalog to the appropriate apparent magnitude limit in a post-processing step.

6. Observed Magnitudes and Photometric Errors

One of the main strengths of the ADDGALS algorithm is its ability to produce photometry in a number of different bands using empirically determined SEDs. In order for these magnitudes to be useful, it is often necessary to include photometric error estimates. These errors cause objects above the detection threshold to scatter out of our detection limits as well as causing many more faint objects to scatter in. Modeling these errors appropriately can thus be important for analyses that use galaxies close to the detection limits of their respective surveys, which is the case for most weak-lensing analyses.

A significant challenge is the construction of an appropriate error model that is consistent between surveys. Existing surveys report limiting magnitudes in several inconsistent ways. For example, some surveys report 5σ galaxy magnitudes, some report 10σ point-source magnitudes, and still others report limiting magnitudes by measuring the 80% completeness limit.

To ensure that errors are consistently defined, we have instead taken a pragmatic approach to calculate galaxy limiting magnitudes. For all existing surveys, we remeasure the 10σ limiting magnitude (m_{lim}) given the reported galaxy

photometric errors using the algorithm described in Rykoff et al. (2015). To match the full magnitude/error distribution, we also measure an effective exposure time (t_{eff}) and an additional parameter (Σ_{int} , described below) to encompass variations in survey depth, seeing, and galaxy size.

Synthetic photometric errors are calculated using a relatively straightforward method of calculating the Poisson noise for the flux of a simulated galaxy plus the sky noise in a particular band. Here, the total signal from these two sources (galaxy and sky) is given by the relation:

$$\begin{aligned} S_{\text{gal}} &= 10^{-0.4(m_{\text{gal}} - ZP)} \times t_{\text{eff}} \\ S_{\text{sky}} &= f_{\text{sky}} \times t_{\text{eff}}, \end{aligned} \quad (12)$$

where m_{gal} is the magnitude of a galaxy, f_{sky} is the sky noise (in a particular band), and t_{eff} is the effective exposure time. In all cases, the zero-point is set to $ZP = 22.5$, and all fluxes in the data tables are converted to nanomaggies such that:

$$m = 22.5 - 2.5 \log_{10} f_{\text{nmgy}}. \quad (13)$$

Finally, we note that the sky noise parameter, f_{sky} , can be estimated from the 10σ limiting magnitude m_{lim} and the associated f_{lim} :

$$f_{\text{sky}} = \frac{f_{\text{lim},1}^2 \times t_{\text{eff}}}{100} - f_{\text{lim},1}, \quad (14)$$

where $f_{\text{lim},1}$ is the 1 second flux at the limiting magnitude given by Equation (12).

Given the galaxy flux and sky flux, in the simplest form, the typical noise associated with each galaxy will be given by a random draw from a distribution of width $\sigma_{\text{flux}} = \sqrt{S_{\text{gal}} + S_{\text{sky}}}$. However, in a simple model to account for variations in galaxy size, survey depth, and seeing, we add in an additional log-normal scatter parameter Σ_{int} . After taking σ_{int} as a random draw from a distribution of width Σ_{int} , we arrive at:

$$\sigma_{\text{flux,tot}} = \exp(\ln \sigma_{\text{flux}} + \sigma_{\text{int}}). \quad (15)$$

For most surveys, the typical value for Σ_{int} is ~ 0.2 – 0.3 , equivalent to a 20%–30% scatter in effective depth. For particular survey applications such as in DeRose et al. (2019a), we use maps of the effective depth variation as a function of sky position in order to more realistically model these variations.

After taking a random draw from a distribution of width $\sigma_{\text{flux,tot}}$ for each galaxy, the total observed flux and error are converted to nanomaggies, such that $f_{\text{nmgy}} = S_{\text{gal,obs}}/t_{\text{eff}}$. Finally, magnitudes and magnitude errors are calculated as:

$$\begin{aligned} m_{\text{obs}} &= 22.5 - 2.5 \log_{10}(f_{\text{nmgy}}) \\ m_{\text{err,obs}} &= \frac{2.5}{\ln(10)} \frac{f_{\text{err,nmgy}}}{f_{\text{nmgy}}}. \end{aligned} \quad (16)$$

We provide galaxy magnitude limits for a number of existing and planned surveys. Table 2 lists all of the survey magnitudes included in our simulations, including the filters and the limiting magnitudes for each filter. The existing surveys included are SDSS DR8 (Aihara et al. 2011), SDSS Stripe 82 co-adds (Annis et al. 2014); Wide-field Infrared Survey Explorer (WISE; Jarrett et al. 2011); Vista Hemisphere Survey (VHS; McMahon et al. 2013), VIDEO (Jarvis et al. 2013), and VIKING (Sutherland 2012); and DES DR2 (DES

Table 2
Survey Limiting Magnitudes

Survey	Limits					
DECam	<i>u</i>	<i>g</i>	<i>r</i>	<i>i</i>	<i>z</i>	<i>Y</i>
DES DR2 10- σ		24.07	23.82	23.11	22.28	20.79
SDSS	<i>u</i>	<i>g</i>	<i>r</i>	<i>i</i>	<i>z</i>	
DR8 ^a	20.4	21.7	21.2	20.8	19.3	
Stripe82 ^a	22.1	23.4	23.1	22.6	21.2	
VISTA	<i>z</i>	<i>Y</i>	<i>J</i>	<i>H</i>	<i>K_s</i>	
VHS ^b			20.1	19.7	19.5	
VIKING ^b	21.6	20.9	20.8	20.2	20.2	
VIDEO	25.7	24.6	24.5	24.0	23.5	
WISE	3.4 μ	4.6 μ				
WISE ^c	17.1	15.7				
LSST	<i>u</i>	<i>g</i>	<i>r</i>	<i>i</i>	<i>z</i>	<i>Y</i>
LSST-1 yr ^d	24.2	25.8	25.9	25.2	24.0	23.15

Notes. All limiting magnitudes are 10 σ AB magnitudes for galaxies unless photometric errors are not provided.

^a Limits appropriate for SDSS model magnitudes used for color measurements.

^b Limits for 2'' aperture-corrected magnitudes. Magnitudes have been converted from Vega to AB such that $z_{AB} = z_{Vega} + 0.52$; $Y_{AB} = Y_{Vega} + 0.62$; $J_{AB} = J_{Vega} + 0.94$; $H_{AB} = H_{Vega} + 1.38$; $K_{s,AB} = K_{s,Vega} + 1.8$.

^c Limits for MAG_AUTO. Magnitudes have been converted from Vega to AB such that $J_{AB} = J_{Vega} + 0.91$; $K_{s,AB} = K_{s,Vega} + 1.85$ (Blanton et al. 2005).

^d Rescaled from proposed 10 yr depth for 5 σ point-source detections.

Collaboration et al. 2021). We also produce magnitudes for LSST, where 1 yr limiting magnitudes are obtained by re-scaling the projected 10 yr depth for 5 σ point-source detections.¹¹

7. Validation against SDSS Data

We now present tests of our magnitude and SED assignment algorithms. Here we focus primarily on the global distribution of galaxy colors, clustering as a function of color, and radial profiles of galaxies around clusters in the local universe, compared to data from SDSS. DeRose et al. (2019a) presents additional tests of the model, including additional comparisons between our synthetic catalogs and observations of galaxy clusters, as well as comparisons of luminous red galaxy populations, high-redshift colors, and photometric redshifts in the DES. All of the comparisons presented in this section use ADDGALS run on the L1 lightcone, producing a quarter sky (10,313.25 square degree) footprint out to $z = 0.32$.

7.1. One-point Statistics

We first investigate the ability of ADDGALS to reproduce color, magnitude, and redshift distributions by comparing with the SDSS main galaxy sample. The left panels of Figure 5 show histograms of observed magnitude counts in griz bands. The ADDGALS catalog is compared to the magnitude-limited SDSS main sample with $m_r < 17.77$, where the error bars shown are computed with jackknife using regions of approximately 200 square degrees. The agreement is good to better than 10% to $r \sim 13$, with similar performance at the same number density in the other bands. The discrepancies seen on

the bright end are a result of the redshift evolution imposed in our input rest-frame luminosity function in order to match DES galaxy number densities as described in DeRose et al. (2019a). The upturns at the faint end in griz where SDSS is very incomplete are sensitive to the assumed photometric error model. The *u* band (not plotted) performs significantly worse as a result of the discrepancies seen in Figure 6, which we believe are largely due to the fact that the SED templates are not fully tuned in to *u*-band data.

The right panel of Figure 5 shows the redshift distribution for galaxies in the simulated catalogs compared with those in the SDSS DR7 main sample, using the same magnitude and redshift cuts as the previous comparison. Error bars are computed using the same jackknife procedure. Again we find good agreement.

The top section of Figure 6 presents the distributions of observed $u - g$, $g - r$, $r - i$, and $i - z$ as a function of M_r in our simulations (blue), compared with those from our training set (black). Also displayed in red are the distributions that are obtained when reconstructing each training sample galaxy's magnitudes using only their KCORRECT coefficients. The same magnitude and redshift cuts applied to the training set are also applied to the ADDGALS catalog. Different rows in this figure show bins of absolute magnitude as indicated by the labels.

Although the SEDs from ADDGALS are selected from a training set of these SDSS galaxies, matches in the global color distribution are not guaranteed. The reason for this is twofold. First, if the joint distribution of M_r and z found in SDSS is not reproduced in our simulations, then even if $p(\text{SED}|M_r)$ is perfect, the observed colors will not be matched by the simulation. Second, KCORRECT coefficients are a lossy compression of galaxy SEDs, and so when these SED representations are integrated over bandpasses, they are not guaranteed to exactly reproduce observed magnitudes and colors.

For $g - r$, $r - i$, and $i - z$, we find very good agreement between SDSS and ADDGALS for all magnitude bins. For $u - g$, the agreement between ADDGALS and SDSS is significantly worse for all magnitudes, with ADDGALS showing a narrower red-sequence that is slightly shifted to low $u - g$ relative to the data. The reason for this discrepancy is that the KCORRECT coefficients that are used to represent the training set SEDs are not fit to the *u* band in SDSS. This means that these SED fits do a worse job at reproducing $u - g$ colors, even when comparing the colors predicted from the template fits to the observed colors on a galaxy-by-galaxy basis in our training set (Blanton et al. 2003a). This is evidenced by the fact that the red lines also show the same disagreement with black. The bottom section of Figure 6 shows joint distributions of $u - g$ and $g - r$, $g - r$ and $r - i$, and $r - i$ and $i - z$ colors. Again we see worse performance in $u - g$ due to the aforementioned issues with KCORRECT model fits, but otherwise the agreement is very good.

7.2. Color-dependent Clustering

We have shown previously in Section 4 that the correlation function of galaxies at a given absolute magnitude can be well matched using ADDGALS. Here we test whether the SED assignment algorithm is able to reproduce clustering as a function of magnitude and color by splitting our simulated samples into red and blue subsamples and comparing again to the SDSS DR7 main galaxy sample.

¹¹ <https://docushare.lsstcorp.org/docushare/dsweb/Get/LPM-17>

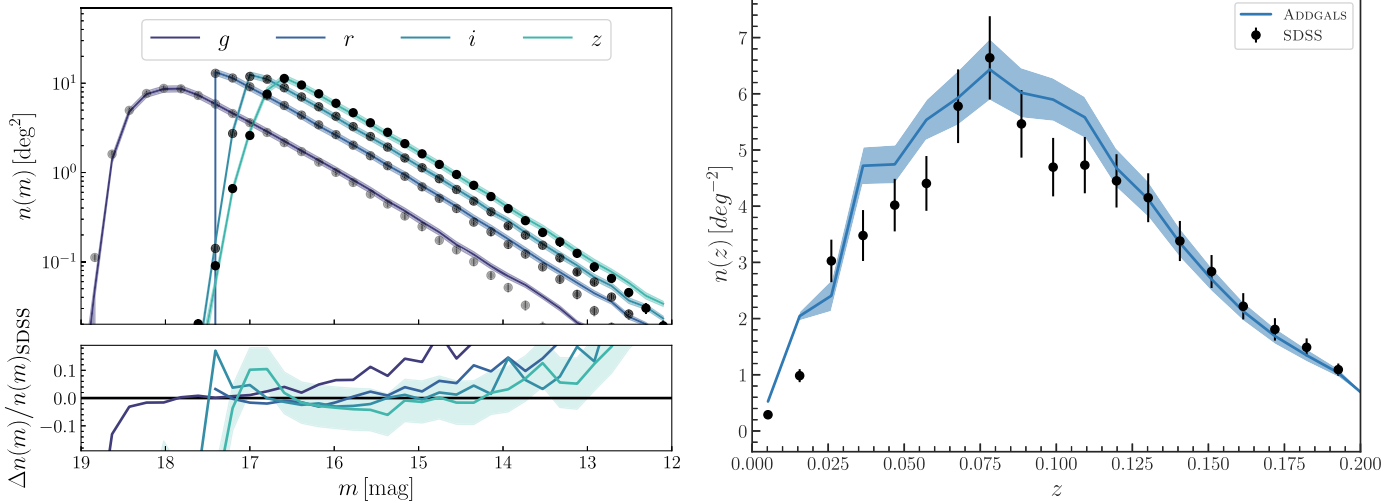


Figure 5. Left: galaxy counts in the SDSS *griz* bands, for all galaxies brighter than $m_r < 17.7$ and at redshifts $z < 0.2$. Black points indicate the SDSS DR7 VAGC sample, and lines are the L1 ADDGALS simulation. Error bars are calculated via jackknife on ~ 200 square degree regions. The bottom panel displays the fractional errors, where we have only plotted error bands once for clarity as they are all of approximately the same size. Right: redshift distribution for simulated galaxies selected to match the SDSS spectroscopic sample, compared to the redshift distribution for galaxies with measured redshifts in the main sample of SDSS DR7. In each case, the galaxies are limited by $14.0 < r < 17.7$ and $0 < z < 0.2$, to match the SDSS training sample used. Error bars are calculated via jackknife on ~ 200 square degree regions.

In Figure 7 we compare our simulations to projected clustering measurements in magnitude bins from Zehavi et al. (2011), adhering to their definition of red galaxies: $g - r > 0.21 - 0.03M_r$. We employ the same $w_p(r_p)$ estimator procedure as outlined in Section 4, but now distributing the randoms uniformly over the unmasked 10,313 square degrees covered by our lightcone simulations, drawing redshifts for our random points to match the distribution of redshifts followed by each galaxy sample separately. The same redshift binning as employed by the SDSS measurements is used for each magnitude bin. Errors on our simulations are estimated via jackknife using ≈ 200 square degree regions.

The trends in the SDSS data are reproduced by our simulations, with red galaxies significantly more clustered than their blue counterparts at fixed M_r . The discrepancies between the red and blue galaxy clustering measurements in our simulations and those in SDSS are largely a consequence of issues with the clustering as a function of M_r , especially for the faintest sample shown. In the bottom panel of this figure, the measurements in the top panel are divided by the $w_p(r_p)$ measurements for samples with the same absolute magnitude selection, but without color selection in order to remove discrepancies caused by issues in the model as a function of M_r alone. Although the fit is not good in a chi-squared sense, we see that most of the discrepancy in the top panel is due to imperfect modeling of clustering as a function of M_r , not our SED assignment algorithm, although red galaxies are still slightly under-clustered with respect to the SDSS measurements.

Despite the reasonable performance exhibited in Figure 7, ADDGALS is not able to reproduce the abundance of galaxy clusters as a function of richness, λ , a common mass proxy used in analyses of REDMAPPER clusters (Roza et al. 2011; Rykoff et al. 2014). To see why this is, Figure 8 compares projected galaxy profiles around REDMAPPER galaxy clusters between ADDGALS and SDSS. The SDSS measurements are taken from Baxter et al. (2017), and our measurements use the same procedure as detailed there. The only difference between

our measurements and the measurements in Baxter et al. (2017) is that the richness cut made on the cluster catalog has been adjusted to $\lambda > 9.3$ rather than $\lambda > 20$ in order to match the abundance of clusters found in SDSS. In doing so, this figure examines galaxy profiles around halos of similar masses in the simulations and SDSS data. Profiles around clusters of the same richness show much better agreement, mostly due to the constraint that equal richness imposes on the projected galaxy number densities at the cluster boundary.

The top panel shows galaxy profiles for three different samples, all galaxies with $M_r < -19.43$ in black, and galaxies in the top and bottom quartiles of the rest frame $g - r$ in red and blue, respectively. At large scales, all profiles agree quite well with the measurements in SDSS, evidencing the fact that the number densities and biases of these samples in SDSS and ADDGALS are very similar. On small scales, all three samples in our simulations exhibit much shallower profiles than seen in the data. The deficits in the red and blue samples are driven entirely by the lack of galaxies in general on these scales, and not an issue with the quenched fraction of galaxies as a function of radius $f_q(r)$. This can be seen more explicitly in the bottom panel, where we divide the red and blue galaxy profiles by the total profiles for the simulations and data, respectively. Here we see that the $f_q(r)$ is actually overpredicted in our simulations for the halo mass range probed by these measurements.

The reason for the deficit in the total galaxy profile is likely artificial subhalo disruption in the T1 simulation, which is then inherited by the ADDGALS model via our training process. Higher-resolution simulations, or an orphan model in the T1 simulation, may help to remedy these issues. Indeed, DeRose et al. (2021a) showed that the inclusion of a model for orphan galaxies can significantly improve the ability of SHAM to fit $M_r < -19$ clustering measurements. This improvement is facilitated by a large increase in galaxy occupation for $M_{\text{vir}} > 10^{13} h^{-1} M_{\odot}$, and as such would also remedy the galaxy number density issues in ADDGALS at the cluster mass scale. This increase in satellite fraction boosts large-scale bias, but

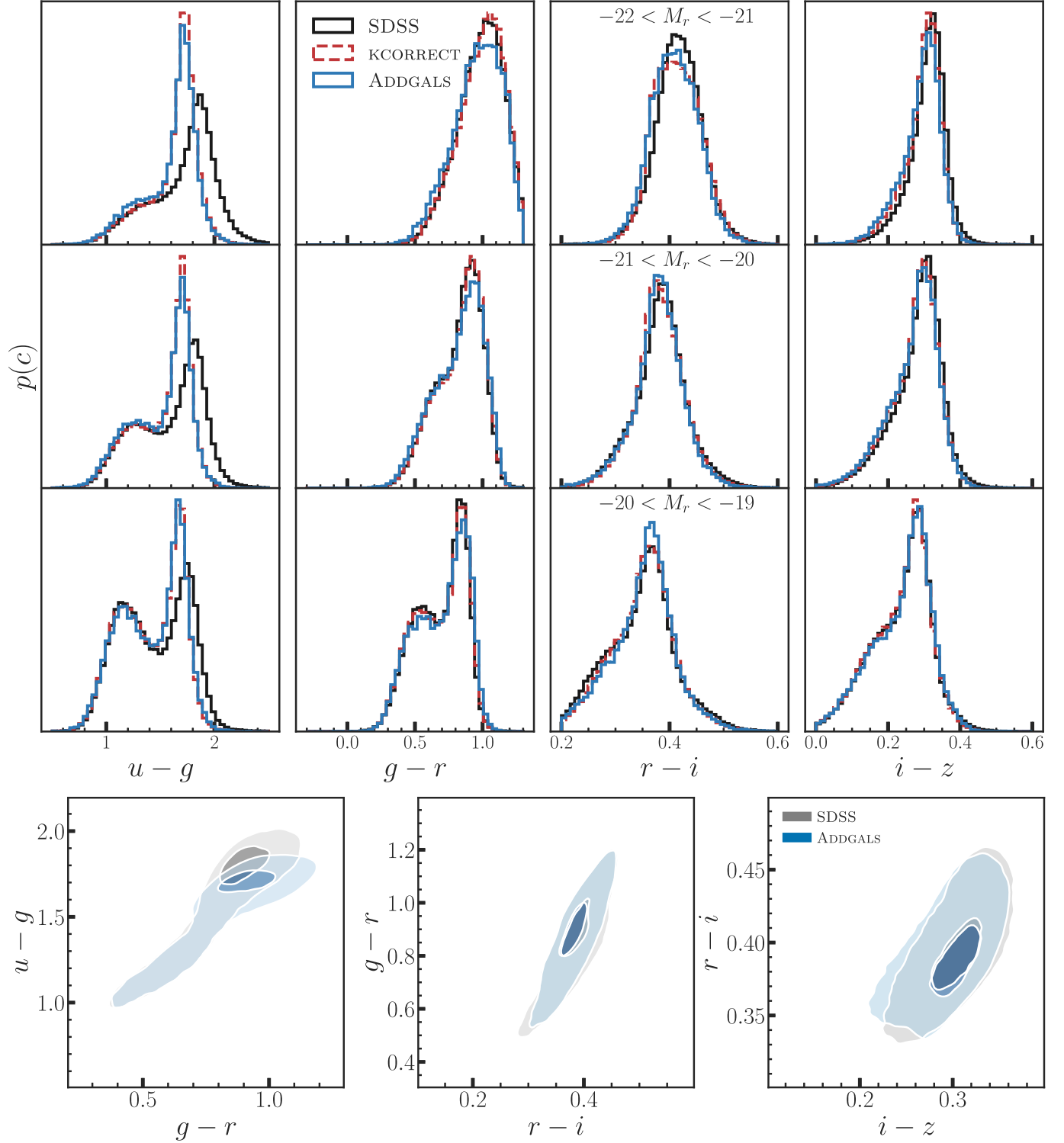


Figure 6. Top: distributions of $u-g$, $g-r$, $r-i$, and $i-z$ colors (columns) in bins of absolute magnitude (rows). In all panels, the black line represents the distribution in SDSS DR7, while the blue lines show the distributions for ADDGALS L1 catalog, and the red dashed lines show the colors predicted from the SDSS DR7 training set if reconstructed from their KCORRECT fits. Nearly all discrepancies between ADDGALS and SDSS are due to inaccuracies in KCORRECT, not our method for assigning SEDs to our simulations, as can be seen by the good match between the blue and red lines. Bottom: color-color distribution for galaxies with $m_r < 17.77$. In both panels, gray contours show measurements from the SDSS DR7 main galaxy sample; blue contours show the ADDGALS catalog. Contours include 39% and 84% of the galaxies.

this is compensated for by a decrease in assembly bias, which has the competing effect of decreasing large-scale bias, while largely maintaining the one-halo clustering signal (see, e.g., the top left panel of Figure 2 in DeRose et al. 2021a). This is

because halos of higher concentration are more biased at this mass scale, and the α parameter of our SHAM model correlates concentration with galaxy luminosity, such that decreasing assembly bias reduces the mean concentration of galaxy host

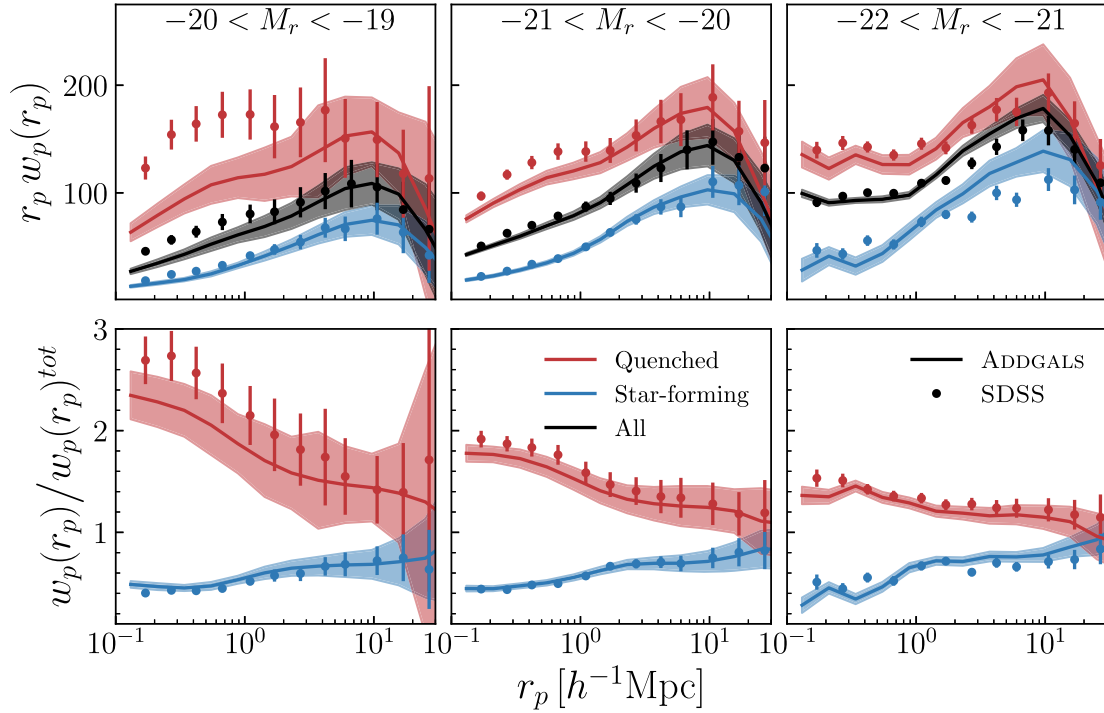


Figure 7. Top: projected galaxy correlation function in magnitude-selected samples for ADDGALS applied to the L1 simulation (lines) compared to the measurements from SDSS (Zehavi et al. 2011; points). Correlation functions binned by M_r only are shown in black; red and blue galaxies are shown in red and blue. Bottom: the red and blue clustering measurements as shown in the top panel divided by the same measurements without color selection for the ADDGALS L1 simulations and the data.

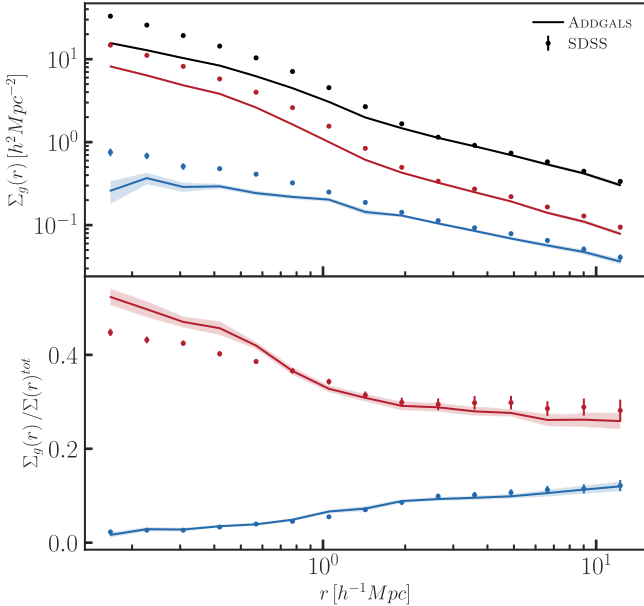


Figure 8. Top: projected galaxy profiles around REDMAPPER clusters for red, blue, and all galaxies with $M_r < -19.43$. Profiles measured in L1 ADDGALS are compared to measurements from Baxter et al. (2017). The deficit in clustering that is seen for all samples is likely due to artificial subhalo disruption in the SHAM model that the ADDGALS model is trained on. This effect is important at larger scales in this measurement than in Figure 3, because it includes higher-mass halos. Bottom: projected galaxy profiles split by color, normalized by the profile for all galaxies. The trends in color are well captured by ADDGALS; although, the quenched fraction $f_q(r)$ is slightly overpredicted at small scales.

halos at fixed absolute magnitude, and thus decreases the large-scale bias. Work is ongoing to incorporate orphan galaxies into the SHAM models that ADDGALS is trained on, but until these improvements are fully implemented, the cluster properties in ADDGALS catalogs must be treated with caution.

8. Resolution Requirements of ADDGALS

Now that we have presented and validated the ADDGALS algorithm, it is important to understand its resolution requirements, as the relatively modest-resolution requirements of the ADDGALS algorithm are one of its major strengths. The left side of Figure 3 compares the projected clustering of ADDGALS run on the $z = 0$ snapshots of three simulations with progressively lower mass resolution, T1, L1, and L2, where the measurements and errors are computed as described in Section 4. In all cases, simulations are converged with respect to the errors on the measurements in the T1 simulation, which has a similar volume to the SDSS main galaxy sample. The L1 and L2 models are also in relatively good agreement, although they show discrepancies at the 10% level on small scales for the $M_r < -22$ sample and 5% for $M_r < -21$ and $M_r < -20$ on scales $r_p < 1 h^{-1} \text{Mpc}$.

The discrepancies between ADDGALS and the SDSS data for the $M_r < -19$ sample are not due to an insufficiency of the ADDGALS algorithm, but rather resolution effects in the SHAM catalog that ADDGALS is trained on. This is demonstrated in the right side of Figure 9, where ADDGALS models trained on two different SHAM models are compared. One is our fiducial SHAM run on the T1 simulation. The other is an SHAM run on the higher-resolution C250 simulation, which was run with the same settings as the T1 simulation, but with a simulation volume of $(250 h^{-1} \text{Mpc})^3$, 2560^3 particles, and a force softening of $\epsilon = 0.8 h^{-1} \text{kpc}$. The clustering of the SHAM C250 model is increased on small scales due to reduced subhalo disruption in the C250 simulation relative to T1. We do not compare to the SDSS data here because the C250 simulation is too small to use the same line-of-sight projection length of $\tau_{\text{max}} = 60$ for $w_p(r_p)$ as used in the data. Instead we use $\tau_{\text{max}} = 20$ for this comparison. Nonetheless it is apparent that the SHAM C250 model would agree with the SDSS

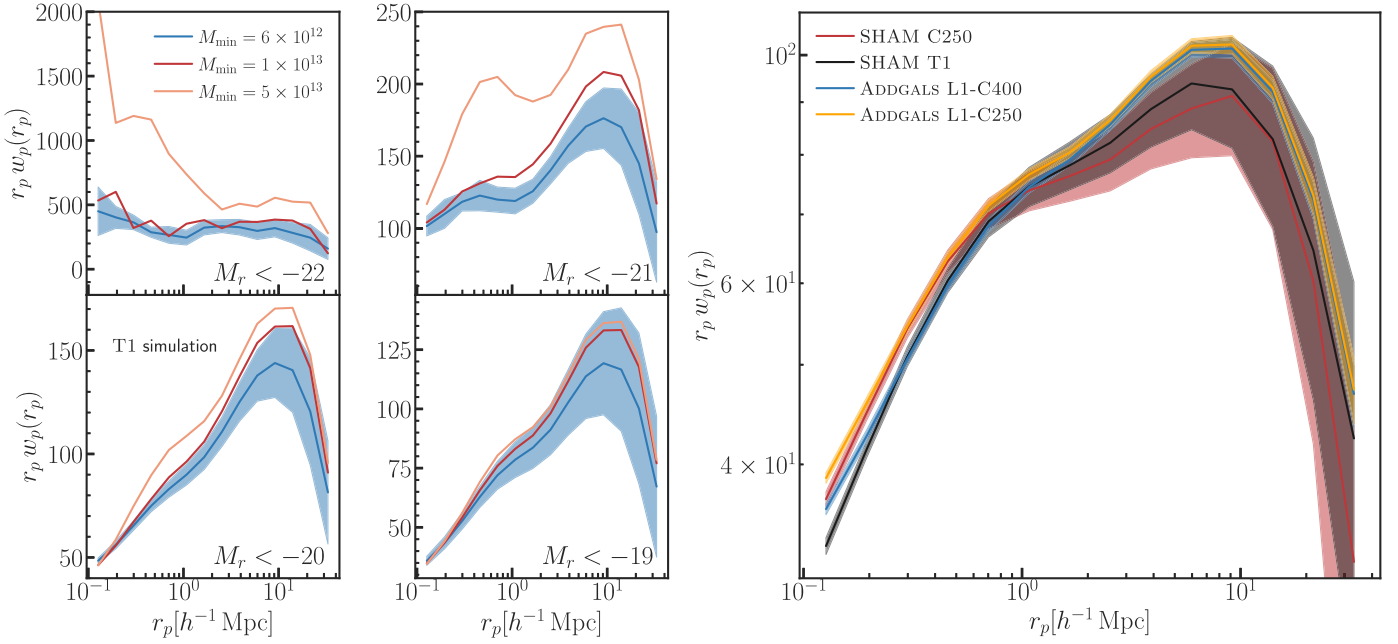


Figure 9. Impact of resolution on galaxy clustering measurements in ADDGALS. Left: projected correlation functions for absolute-magnitude-limited samples of $M_r < -22$, -21 , -20 , -19 for ADDGALS models, varying the minimum mass halo mass, M_{\min} , used to populate central galaxies. This is the parameter that our models are most sensitive to, and largely drives the resolution requirements for ADDGALS. Right: projected correlation functions for $M_r < -19$ samples, varying the resolution of the input simulation used for the SHAM model. The default T1 simulation (black) is compared to a higher-resolution C250 simulation (red); the latter model has stronger clustering below $\sim 1 h^{-1} \text{Mpc}$ due to reduced artificial subhalo disruption. The ADDGALS model trained on this simulation, ADDGALS L1-C250 (yellow), also inherits this increased clustering compared to the default ADDGALS L1-C400 model (blue).

measurements on small scales. The ADDGALS model trained on the SHAM C250 also inherits this increased clustering on small scales. This suggests that with a sufficiently high-resolution training simulation, or an orphan model that traces substructure effectively until it is physically disrupted, ADDGALS could reproduce the small-scale clustering of an $M_r < -19$ sample using a simulation with the resolution of the L1 or even L2 simulation.

In practice, the more important parameter governing the convergence of the ADDGALS method for projected two-point functions is the minimum mass to which central galaxies are populated, M_{\min} . This can be seen in on the left side of Figure 9. All catalogs included in this figure are run on the T1 simulation, varying M_{\min} between our fiducial value of 6×10^{12} and $5 \times 10^{13} h^{-1} M_{\odot}$ as indicated in the legend of the figure but keeping all other parameters fixed. In most cases, the shifts are smaller than the errors on the measurements, but it is clear that this parameter is a very important free parameter of the ADDGALS algorithm, especially for brighter samples. The dependence on this parameter hints at a breakdown in the bright galaxy regime of our assumption that matching $p(R_{\delta}|M_r, z)$ of an SHAM is sufficient to reproduce $w_p(r_p)$ in that SHAM, since even for a high-resolution simulation such as T1, significant discrepancies in clustering are produced when too many bright galaxies are populated using this relation, whereas faint galaxies are much less affected. This breakdown is sourced by the fact that $p(R_{\delta}|M_{\text{vir}}, M_r, \text{central})$ does not evolve significantly for $M_{\text{vir}} > 10^{13} h^{-1} M_{\odot}$ for bright galaxies. As such, if we do not place centrals in halos by $M_{\text{vir}} > 10^{13} h^{-1} M_{\odot}$, then using $p(R_{\delta}|M_r, z)$ induces significant scatter in M_{vir} , placing galaxies that should have been centrals of lower-mass halos as satellites in high-mass halos, thus significantly boosting the clustering signals for bright galaxies as seen in the left-hand side of Figure 9. The exact halo mass that we must

populate central galaxies down to very likely depends on the mass used to compute R_{δ} , but we have not explored this dependence in detail.

Finally, we expect ADDGALS to fail for simulations where the mass scale used to define R_{δ} is too coarsely resolved by the particle resolution. In this regime, the density estimates produced by R_{δ} will not consistently measure similar environments in the training volumes versus the volumes used for the synthetic catalogs. As simulations of this low resolution are increasingly irrelevant due to advances in computational power, we have not explored this effect in detail.

9. Conclusions

We present the ADDGALS algorithm, designed to produce realistic simulated galaxy populations with only a modest computational cost. To achieve this goal, we employ a combination of empirical models of galaxy-halo connection in high-resolution simulations with a custom, physically motivated machine-learning model that is trained to place galaxies into lower-resolution volumes. This combination of techniques, which explicitly incorporates key statistical information from the data (e.g., the luminosity function and the distribution of colors/SED types), lends a baseline level of realism to the output catalog. In this work, we show that we are able to match several characteristics of the input training catalog, including matching the clustering properties of the input empirical model as a function of r -band absolute magnitude and redshift. We also demonstrate that we can produce realistic color distributions and can reproduce the most significant trends in clustering as a function of color. Several further comparisons are presented in DeRose et al. (2019a), which additionally describes associated weak-lensing catalogs, additional redshift evolution, and tests photometric redshift and

cluster finding methodology in higher-redshift synthetic surveys.

The modest simulation requirements of this method have enabled us to produce volumes of synthetic sky surveys that would be significantly more computationally expensive with other methods in active use. This includes, for example, the ability to produce the large and deep sky areas appropriate for modeling modern photometric surveys like DES, LSST, Euclid, and the Roman Space Telescope surveys. The catalogs created with the ADDGALS method have been used for a wide variety of applications including tests of photometric redshift, clustering, weak lensing, cross-correlation, and cluster finding methodology. In companion papers, the modest computational cost has allowed us to produce a significant number of such catalogs, e.g., tens of full area and depth realizations, which have been used to statistically test the performance of precision cosmological probes in the DES (MacCrann et al. 2018; DeRose et al. 2019a, 2021b).

One of the distinguishing features of ADDGALS’ machine-learning model is that it uses a hand-crafted parameterization as opposed to a more generic functional form (e.g., a tree ensemble or neural network). This parameterization is constructed specifically to fit the simulation data, especially near the tails of the distribution where some extrapolation is needed. Looking ahead, generalizations of the ADDGALS algorithm that employ more traditional machine-learning models may be able to achieve better performance, but it is likely that special attention will need to be paid to how these models extrapolate beyond the training data. This lesson is likely quite general for any machine-learning model of this type, given that high-resolution simulations typically sample less volume of the universe than lower-resolution ones.

This method is not without limitations. In particular, it has difficulty precisely reproducing the small-scale clustering measured from SDSS of the faintest galaxy samples considered in this paper. This issue is likely inherited from artificial subhalo disruption in the simulation that ADDGALS is trained on. This deficit in clustering leads to a low normalization of the HOD and a deficit of galaxies at the cores of cluster mass halos with respect to observations (DeRose et al. 2019a). The realistic properties of galaxy cluster populations do enable us to run modern cluster finders on the simulated data, but the lack of galaxies in the central regions of massive groups and clusters leads to an offset in the mass–richness relation that can hinder some use cases related to important cluster selection systematics. This can be remedied with the inclusion of orphan galaxies in our SHAM model, and this work is currently being undertaken.

Additionally, our SED assignment algorithm requires a representative sample of observed galaxies from which to draw SEDs in order to accurately reproduce galaxy colors. If there are SEDs that appear at high redshift, or fainter absolute magnitudes, that are not present in our low-redshift SDSS training set, then the assumptions used by ADDGALS to populate SEDs will be broken. We showed here that in the local universe, these assumptions can also be broken outside the wavelength range where the SED templates are well tuned, and we urge some caution for this reason in using bands outside of the rest frame g through Y bands. For a discussion of the extent to which these assumptions are broken in DES, see DeRose et al. (2019a). We expect that significant progress can

be made in these areas especially using data from larger, deeper spectroscopic surveys to train the model.

A final significant issue with this methodology compared to more accurate methods based on fully resolved halo substructures and their histories (including hydrodynamical models, SAMs, or empirical models based on high-resolution merger trees) is that it may lack important correlations that are expected in such models. These could include, for example, the correlated properties of both central and satellite galaxies with each other and with the larger-scale environment.

Given the size of ongoing and upcoming surveys, and their demands for accurate reproduction of galaxy magnitudes, colors, and spatial clustering, it is likely that techniques that combine empirical methods with machine-learning methods in order to reduce computational cost will remain a necessary tool for precision cosmology for the foreseeable future. They will also provide a very useful complement to higher-fidelity simulations that can be produced over smaller volumes. It is thus worth considering how to mitigate some of the limitations discussed above, and active work in each of these areas is ongoing.

ADDGALS data, including a one-quarter sky simulation out to $z = 2.35$ to a depth of $r = 27$, with magnitudes appropriate for modeling several surveys including SDSS, DES, VISTA, WISE, and LSST, are available at <http://www.slac.stanford.edu/~risa/addgals>.

R.H.W. thanks her many collaborators for near infinite patience on the completion of this paper, which was begun in another era. We thank Rachel Reddick, Alex Ji, and our collaborators on the maxBCG team and in the DES collaboration, especially Chihway Chang, Carlos Cunha, Joerg Dietrich, Sarah Hansen, Brandon Erickson, Daniel Gruen, Benjamin Koester, Niall MacCrann, Chris Miller, Eduardo Rozo, Erin Sheldon, Tim McKay, and Molly Swanson, for significant useful feedback on several earlier versions of these catalogs. We thank Andreas Berlind, Derek Bingham, Joanna Dunkley, Andrew Hearin, Andrey Kravtsov, Yao-Yuan Mao, Hiranya Peiris, Eduardo Rozo, Frank van den Bosch, and Martin White for useful discussions about methodology and statistical inference during early development. This work received support from the U.S. Department of Energy under contract No. DE-AC02-76SF00515 at SLAC National Accelerator Laboratory, the Kavli Institute for Particle Astrophysics and Cosmology, and a Terman Fellowship at Stanford University. J.D. is supported by the Chamberlain Fellowship at Lawrence Berkeley National Laboratory. Argonne National Laboratory’s work was supported by the U.S. Department of Energy, Office of Science, Office of Nuclear Physics, under contract DE-AC02-06CH11357.

This research used resources of the National Energy Research Scientific Computing Center (NERSC), a U.S. Department of Energy Office of Science User Facility located at Lawrence Berkeley National Laboratory, operated under contract No. DE-AC02-05CH11231. Some of the computing for this project was performed on the Sherlock cluster, and on computing resources at SLAC National Accelerator Laboratory. We would like to thank Stanford University and the Stanford Research Computing Center for providing computational resources and support that contributed to these research results. We are grateful to Stuart Marshall and the rest of the SLAC computing team for extensive support of this work.

This study made use of the SDSS DR7 Archive (as well as earlier versions while the model was in development), for which funding has been provided by the Alfred P. Sloan Foundation, the Participating Institutions, the National Aeronautics and Space Administration, the National Science Foundation, the U.S. Department of Energy, the Japanese Monbukagakusho, and the Max Planck Society. The SDSS Web site is <http://www.sdss.org/>. The SDSS is managed by the Astrophysical Research Consortium (ARC) for the Participating Institutions: the University of Chicago, Fermilab, the Institute for Advanced Study, the Japan Participation Group, the Johns Hopkins University, Los Alamos National Laboratory, the Max-Planck-Institute for Astronomy (MPIA), the Max-Planck-Institute for Astrophysics (MPA), New Mexico State University, University of Pittsburgh, Princeton University, the United States Naval Observatory, and the University of Washington. The authors acknowledge the support and stimulating environments of the Aspen Center for Physics and the Kavli Institute for Theoretical Physics (under NSF grant No. 1748958) where some of this work was performed.

Software: ROCKSTAR (Behroozi et al. 2013b), GADGET2 (Springel et al. 2005), 2LPTIC (Crocce et al. 2006), CAMB code (Lewis 2004).

Appendix A

Constructing the Training Galaxy Catalog with Subhalo Abundance Matching

In this work, we use subhalo abundance matching (SHAM; e.g., Conroy et al. 2006; Behroozi et al. 2010; Wetzel & White 2010; Reddick et al. 2013; Lehmann et al. 2017) to construct the training data for the ADDGALS model. Specifically, we employ the model described in Lehmann et al. (2017), placing galaxies into resolved halos and subhalos by matching the number density of galaxies as a function of absolute magnitude with that of the dark matter halos or subhalos as a function of $v_\alpha = v_{\text{vir}} \left(\frac{v_{\text{max}}}{v_{\text{vir}}} \right)^\alpha$. The quantities v_{max} and v_{vir} are evaluated in this equation at the time when the halo is accreted onto a larger halo. We take $\alpha = 0.684$ and $\sigma(M_r | v_\alpha) = 0.425$. The parameter α can be thought of as determining the concentration dependence of a halo's rank ordering, with larger α giving higher-concentration halos a higher rank at fixed mass. The choice to evaluate the velocities used to calculate v_α at the epoch when the halo is accreted onto a larger halo is based on the idea that a galaxy's stellar mass should be much less susceptible to stripping than the outer regions of its dark matter halo (Conroy et al. 2006; Reddick et al. 2013).

SHAM models generally require a single observational input, the redshift-dependent galaxy luminosity function (LF) in a given band. We find that a pure Schechter function is insufficient to model galaxy luminosities for our purposes. At bright luminosities, there are significantly more galaxies than a pure exponential model would predict (see, e.g., Blanton et al. 2003b; Bernardi et al. 2013). In particular, the steep bright-end slope of a Schechter function results in a very flat mass–luminosity relation for brightest-cluster galaxies when using abundance matching, a relation that is inconsistent with observations (e.g., Hansen et al. 2009; Kravtsov et al. 2018; To et al. 2020). Using a luminosity function that more closely matches observations relieves this tension.

Table 3

Parameters of the SDSS DR7 r -band $z = 0.05$ Luminosity Function as Defined by Equation (17)

ϕ_1	$0.0156 \pm 0.03h^{-1} \text{ Mpc}$
ϕ_2	$0.00671 \pm 0.00029h^{-1} \text{ Mpc}$
α_1	-0.166 ± 0.041
α_2	-1.523 ± 0.01
M_*	$-19.88 \pm 0.03 - 5 \log(h)$
ϕ_3	$(3.08 \pm 3.24) \times 10^{-5} h^{-1} \text{ Mpc}$
M_{hi}	$-21.72 \pm 0.52 - 5 \log(h)$
σ_{hi}	0.484 ± 0.192

We measure the luminosity function directly using data in the SDSS DR7 VAGC, using the same method outlined in Reddick et al. (2013). To this measurement, we fit a modified double-Schechter function with a Gaussian at the bright end, as given by

$$\begin{aligned} \Phi(M) = & 0.4 \ln(10) e^{-10^{-0.4(M-M_*)}} \phi_1 10^{-0.4(M-M_*)(\alpha_1+1)} \\ & + 0.4 \ln(10) e^{-10^{-0.4(M-M_*)}} \phi_2 10^{-0.4(M-M_*)(\alpha_2+1)} \\ & + \frac{\phi_3}{\sqrt{2\pi\sigma_{hi}^2}} e^{-\frac{(M-M_{hi})^2}{2\sigma_{hi}^2}}. \end{aligned} \quad (17)$$

At $z = 0.05$, we find that Equation (17) with parameters listed in Table 3 reproduces the observations extremely well. We also include evolution in this luminosity function with redshift by allowing for evolution in ϕ_i , M_* , and M_{hi} of the form:

$$M_{*/hi}(z) = M_{*/hi,0} + Q \left(\frac{1}{1+z} - \frac{1}{1.1} \right), \quad (18)$$

and

$$\phi_i(z) = \phi_{i,0} + Pz. \quad (19)$$

The value of P is taken from Cool et al. (2012), but Q is fit to match counts as a function of magnitude from DES Y1 data. This evolution is constrained to be very small over the redshift range relevant to the current work. We refer readers to DeRose et al. (2019a) for more details related to how this evolution is constrained.

With the luminosity function above, we use SHAM to populate all 100 snapshots of the T1 simulation. Our catalogs are complete down to roughly $M_r - 5 \log(h) = -19$ in the T1 simulation and provide an excellent fit to the observed SDSS magnitude dependent two-point correlation function as measured in Reddick et al. (2013). A comparison of the SHAM algorithm applied to the T1 simulation with SDSS data is shown in Figure 3, and is described further in Section 4.

Appendix B

Modeling $p(R_\delta | M_r, z)$

In order to determine $\Theta(x, z)$ (see Equation (7)), R_δ is measured at the position of each galaxy in the SHAM catalogs. The function $\hat{p}(R_\delta | M_r < x_i, z_j)$ is then determined, where the hat denotes that this is a measured quantity in the i th magnitude bin and j th snapshot, using magnitude bins with width $\Delta M_r = 0.1$ between $-23 < x_i < -18$ in the 56 snapshots with $z_j < 2.5$. $\hat{p}(R_\delta | M_r < x_i, z_j)$ is used rather than $\hat{p}(R_\delta | M_r = x_i, z_j)$, because the former quantity is significantly less noisy

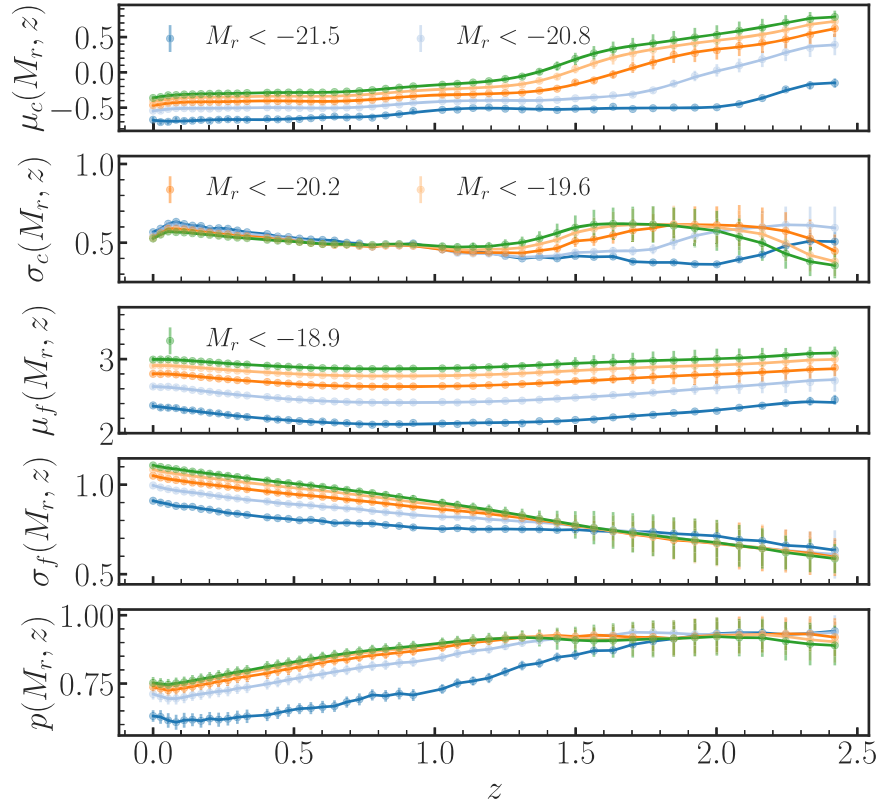


Figure 10. Parameters of the model for $p(R_\delta|M_r, z)$, σ_c , σ_f , μ_c , μ_f , and p , as a function of redshift and magnitude. Lines show the Gaussian process model for this redshift and magnitude dependence.

for bright magnitudes, and we have found that this allows for more robust estimation of the parameters in Equation (7).

Equation (7) is then fit to each magnitude cut, x_i , and redshift, z_j . In practice, we do not fit for Θ , instead opting to perform the fit in a basis where the parameters have minimal covariance. To achieve this, $\hat{p}(R_\delta | M_r < x_i, z_j)$ is first fit using the original set of parameters, Θ , maximizing the likelihood given by

$$\mathcal{L} = \mathcal{N}(\hat{p}(R_\delta | M_r < x_i, z_j) - p(R_\delta ; \Theta(x, z)), \hat{\Sigma}_{i,j}), \quad (20)$$

where $\hat{\Sigma}_{i,j}$ is the covariance matrix of $\hat{p}(R_\delta | M_r < x_i, z_j)$ between each R_δ bin. The covariance matrix is estimated via jackknife using 125 equal volume subregions of the T1 simulation. This procedure allows for the estimation of the parameter covariance matrix, \bar{T} , as the mean of the parameter covariance matrices for each redshift and magnitude bin, $T_{i,j}$.

The function $\hat{p}(R_\delta | M_r < x_i, z_j)$ is then fit to each magnitude and redshift bin again, this time performing the maximization over the parameter space defined by

$$\Theta' = \bar{P}\Theta, \quad (21)$$

where \bar{P} is the change of basis matrix that diagonalizes \bar{T} , yielding a set of estimated parameters for each magnitude and redshift bin, $\Theta'_{i,j}$. In order to smoothly interpolate between these as a function of M_r and z , a Gaussian process is fit to the set of $\Theta'_{i,j}$. With the Gaussian process model, $\hat{\Theta}'(x, z)$, it is possible to predict $p(R_\delta | M_r < x, z) = p(R_\delta ; T^{-1}\hat{\Theta}'(x, z))$. Figure 10 shows the Gaussian process fits to the parameters of this

model, and shows the parameter trends with redshift and magnitude.

Appendix C Sampling from $p(R_\delta|M_r, z)$

Here we describe how we draw samples of densities, R_δ , from $p(R_\delta|M_r, z)$, where M_r and z are the absolute magnitude and redshift of a galaxy in our simulation. It is trivial to convert random samples from a uniform distribution into samples from an arbitrary one-dimensional probability distribution function, using the cumulative distribution function (CDF) of the PDF, which can be obtained by numerically integrating the CDF. The difficulty in our case is that we do not have direct access to $p(R_\delta|M_r, z)$, but rather to $p(R_\delta|M_r < x, z)$, since this quantity can be measured with significantly less noise in our simulations than $p(R_\delta|M_r, z)$. This is particularly true for the brightest galaxies since there are few of these in the training simulation. Because we know the average luminosity function in our training simulation, we can convert $p(R_\delta|M_r < x, z)$ to $p(R_\delta|M_r, z)$ using:

$$p(R_\delta|M_r) = \frac{1}{Z} [N(x + \delta M_r)p(R_\delta|M_r < x + \delta M_r) - N(x)p(R_\delta|M_r < x)] \quad (22)$$

$$= \frac{\mathcal{I}(R_\delta|M_r)}{Z}, \quad (23)$$

where

$$Z = \int dR_\delta \mathcal{I}(R_\delta | M_r). \quad (24)$$

We have dropped the z argument to all functions for legibility, and where $N(M_r) = \int_{-\infty}^{M_r} dM'_r \phi(M'_r)$ is the cumulative number density of all galaxies brighter than M_r . In practice, we evaluate $p(R_\delta | M_r, z)$ on a grid of redshift and absolute magnitude using Equation (22). For the i th galaxy, we choose the grid point

nearest to $M_{r,i}$ and z_i and sample from the appropriate $p(R_\delta | M_r, z)$ to draw a density.

Appendix D Halo Occupation Statistics in ADDGALS

Here we discuss the halo occupation statistics of the ADDGALS method compared to the SHAM model, applied to the T1 high-resolution training simulation. The top-left panel of Figure 11 shows a comparison of the $p(M_{r,\text{cen}} | M_{\text{halo}})$ as measured in the

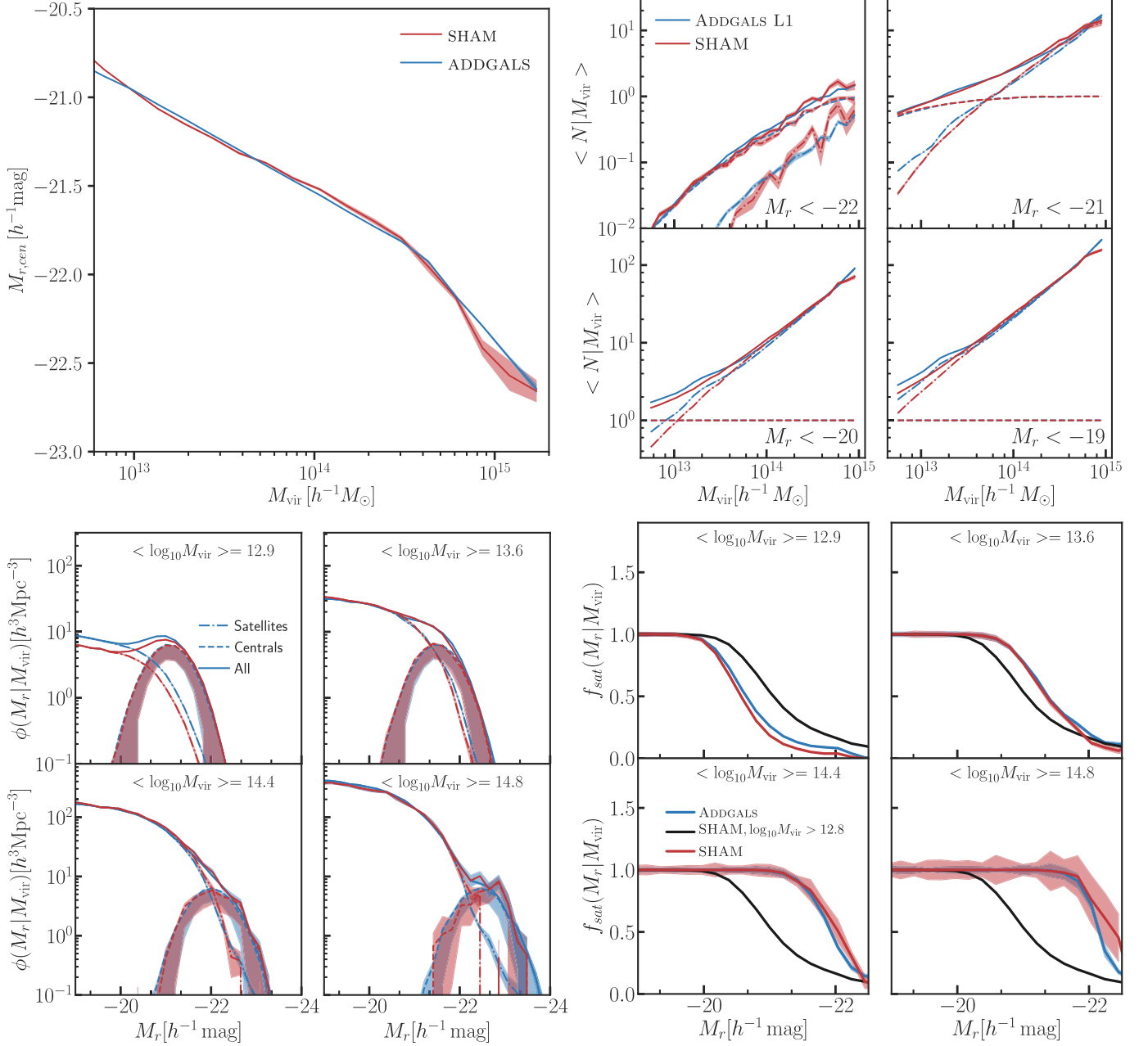


Figure 11. Comparison of halo occupation statistics between the ADDGALS L1 model (blue) and the SHAM model it is tuned to (red; based on the T1 simulation). Top left: central galaxy r -band absolute magnitude as a function of host halo mass. Top right: HOD for four magnitude-limited samples. The solid lines show total HODs, the dashed lines show central HODs, and the dashed-dotted lines show satellite HODs. Error bars shown are the jackknife error bars for each catalog. Bottom left: conditional luminosity function (CLF) for four bins in halo mass (the average $\log(h^{-1} M_\odot)$ in the bin is labeled in each panel). The dashed lines are central luminosity functions, the dashed-dotted lines are satellite luminosity functions, and the solid lines are the sum of the two. Error bars indicate the jackknife error bars for each catalog. Bottom right: satellite fraction for galaxies in halos in four mass bins as a function of r -band absolute magnitude. For reference, the black line shows the satellite fraction in the T1 SHAM catalog for all halos with $\log_{10} M_{\text{vir}} > 12.8$.

$z = 0$ snapshot of the T1 SHAM catalog and the relation in an ADDGALS catalog run on the $z = 0$ snapshot of the L1 simulation. The agreement seen here is validation that the model in Equation (1) describes this relation well. The small discrepancies seen at the bright end can be explained by differences in the assumed functional forms. The ADDGALS model for $M_{r,\text{cen}}(M_{\text{vir}})$ is a broken power law, which does not perfectly fit the relation measured in the SHAM model at the bright end. The luminosity function employed when creating the SHAM catalog assumes a Schechter function plus a Gaussian component at the bright end, and the Gaussian component leads to a deviation from a power law for $M_r < -22$. The functional form for $M_{r,\text{cen}}(M_{\text{vir}})$ used in ADDGALS was derived in Vale & Ostriker (2004) assuming a pure Schechter function, and is fit well by a pure power law for $M_r < -22$. This difference may give rise to slight discrepancies in the probability that the brightest galaxy in a cluster mass halo is the central galaxy between the SHAM and ADDGALS models.

We compare the HODs and conditional luminosity functions (CLFs) measured in the SHAM and ADDGALS catalogs. Since SHAM has been shown to provide a good match to the observed CLF (Reddick et al. 2013), this comparison tests the assumption that the $p(R_\delta|M_r, z)$ relation is sufficient to recover a range of properties of the galaxy distribution and its relation to the underlying halos. In the top-right panels of Figure 11, we compare the HOD as measured in the ADDGALS L1 catalog and the SHAM catalog. ADDGALS largely agrees with the SHAM catalog, with some minor differences appearing around $10^{13}h^{-1}M_\odot$, where ADDGALS overpredicts abundances of galaxies with respect to SHAM. The reason for this is because at masses below the smoothing scale used to measure R_δ (i.e., $1.8 \times 10^{13}h^{-1}M_\odot$), $P(R_\delta|M_r)$ becomes much broader and thus is less able to disambiguate between halos of different masses. Due to the power-law halo mass function at low mass, galaxies that should have been placed in low-mass halos can then scatter into higher-mass halos, leading to the excess seen in the ADDGALS HOD measurements compared with the SHAM HODs.

The bottom-left panel of Figure 11 shows a comparison of the CLF of galaxies in bins of halo mass. Again, ADDGALS and the SHAM catalog are largely in agreement with each other, except for the lowest-mass bin we consider, where a similar Eddington-like bias is at play. The bottom-right panel of Figure 11 shows a comparison of the fraction of galaxies that are satellites as a function of magnitude in the same mass bins as those used to measure the CLF. The satellite fraction for all galaxies in halos with $M_{\text{vir}} > 5 \times 10^{12}h^{-1}M_\odot$ is included in black for reference. At bright magnitudes, ADDGALS slightly overpredicts the satellite fraction in the lowest-mass bin shown, and slightly underpredicts the bright-end satellite fraction for more massive halos, but these differences are small.

ORCID iDs

Risa H. Wechsler  <https://orcid.org/0000-0003-2229-011X>
 Joseph DeRose  <https://orcid.org/0000-0002-0728-0960>
 Matthew R. Becker  <https://orcid.org/0000-0001-7774-2246>
 Eli Rykoff  <https://orcid.org/0000-0001-9376-3135>
 August Evrard  <https://orcid.org/0000-0002-4876-956X>

References

Abbott, T. M. C., Abdalla, F. B., Alarcon, A., et al. 2018, *PhRvD*, **98**, 043526
 Abbott, T. M. C., Aguena, M., Alarcon, A., et al. 2020, *PhRvD*, **102**, 023509
 Aihara, H., Allende Prieto, C., An, D., et al. 2011, *ApJS*, **193**, 29

Anbajagane, D., Evrard, A. E., Farahi, A., et al. 2020, *MNRAS*, **495**, 686
 Annis, J., Soares-Santos, M., Strauss, M. A., et al. 2014, *ApJ*, **794**, 120
 Asorey, J., Carrasco Kind, M., Sevilla-Noarbe, I., Brunner, R. J., & Thaler, J. 2016, *MNRAS*, **459**, 1293
 Avila, S., Murray, S. G., Knebe, A., et al. 2015, *MNRAS*, **450**, 1856
 Balaguera-Antolínez, A., Kitaura, F.-S., Pellejero-Ibáñez, M., Zhao, C., & Abel, T. 2019, *MNRAS*, **483**, L58
 Baxter, E., Chang, C., Jain, B., et al. 2017, *ApJ*, **841**, 18
 Becker, M. R. 2015, arXiv:1507.03605
 Becker, M. R., McKay, T. A., Koester, B., et al. 2007, *ApJ*, **669**, 905
 Becker, M. R., Troxel, M. A., MacCrann, N., et al. 2016, *PhRvD*, **94**, 022002
 Behroozi, P., Wechsler, R. H., Hearin, A. P., & Conroy, C. 2019, *MNRAS*, **488**, 3143
 Behroozi, P. S., Conroy, C., & Wechsler, R. H. 2010, *ApJ*, **717**, 379
 Behroozi, P. S., Wechsler, R. H., & Conroy, C. 2013a, *ApJ*, **770**, 57
 Behroozi, P. S., Wechsler, R. H., & Wu, H.-Y. 2013b, *ApJ*, **762**, 109
 Behroozi, P. S., Wechsler, R. H., Wu, H.-Y., et al. 2013c, *ApJ*, **763**, 18
 Benson, A. J. 2012, *NewA*, **17**, 175
 Benson, A. J., Frenk, C. S., Lacey, C. G., Baugh, C. M., & Cole, S. 2002, *MNRAS*, **333**, 177
 Berger, P., & Stein, G. 2019, *MNRAS*, **482**, 2861
 Berlind, A. A., & Weinberg, D. H. 2002, *ApJ*, **575**, 587
 Bernardi, M., Meert, A., Sheth, R. K., et al. 2013, *MNRAS*, **436**, 697
 Blanton, M. R., Brinkmann, J., Csabai, I., et al. 2003a, *AJ*, **125**, 2348
 Blanton, M. R., Hogg, D. W., Bahcall, N. A., et al. 2003b, *ApJ*, **592**, 819
 Blanton, M. R., Schlegel, D. J., Strauss, M. A., et al. 2005, *AJ*, **129**, 2562
 Bleem, L. E., Stalder, B., de Haan, T., et al. 2015, *ApJS*, **216**, 27
 Bleem, L. E., van Engelen, A., Holder, G. P., et al. 2012, *ApJ*, **753**, L9
 Bond, J. R., & Myers, S. T. 1996, *ApJS*, **103**, 1
 Bonnett, C., Troxel, M. A., Hartley, W., et al. 2016, *PhRvD*, **94**, 042005
 Bower, R. G., Benson, A. J., Malbon, R., et al. 2006, *MNRAS*, **370**, 645
 Bradshaw, A. K. 2019, AAS Meeting Abstracts, **233**, 376.01
 Bryan, G. L., & Norman, M. L. 1998, *ApJ*, **495**, 80
 Buchs, R., Davis, C., Gruen, D., et al. 2019, *MNRAS*, **489**, 820
 Bullock, J. S., Wechsler, R. H., & Somerville, R. S. 2002, *MNRAS*, **329**, 246
 Cai, Y.-C., Angulo, R. E., Baugh, C. M., et al. 2009, *MNRAS*, **395**, 1185
 Cawthon, R., Davis, C., Gatti, M., et al. 2018, *MNRAS*, **481**, 2427
 Cawthon, R., Elvin-Poole, J., Porredon, A., et al. 2020, arXiv:2012.12826
 Chang, C., & Jain, B. 2014, *MNRAS*, **443**, 102
 Chang, C., Pujol, A., Mawdsley, B., et al. 2018, *MNRAS*, **475**, 3165
 Chang, C., Vikram, V., Jain, B., et al. 2015, *PhRvL*, **115**, 051301
 Chaves-Montero, J., Angulo, R. E., Schaye, J., et al. 2016, *MNRAS*, **460**, 3100
 Chuang, C.-H., Kitaura, F.-S., Prada, F., Zhao, C., & Yepes, G. 2015, *MNRAS*, **446**, 2621
 Clampitt, J., Sánchez, C., Kwan, J., et al. 2017, *MNRAS*, **465**, 4204
 Cole, S., Lacey, C. G., Baugh, C. M., & Frenk, C. S. 2000, *MNRAS*, **319**, 168
 Conroy, C., Wechsler, R. H., & Kravtsov, A. V. 2006, *ApJ*, **647**, 201
 Contreras, S., Angulo, R., & Zennaro, M. 2021, *MNRAS*, **508**, 175
 Cool, R. J., Eisenstein, D. J., Kochanek, C. S., et al. 2012, *ApJ*, **748**, 10
 Cooray, A. 2006, *MNRAS*, **365**, 842
 Crocce, M., Castander, F. J., Gaztañaga, E., Fosalba, P., & Carretero, J. 2015, *MNRAS*, **453**, 1513
 Crocce, M., Pueblas, S., & Scoccimarro, R. 2006, *MNRAS*, **373**, 369
 Croton, D. J., Stevens, A. R. H., Tonini, C., et al. 2016, *ApJS*, **222**, 22
 Cunha, C. E., Huterer, D., Busha, M. T., & Wechsler, R. H. 2012, *MNRAS*, **423**, 909
 Cunha, C. E., Huterer, D., Lin, H., Busha, M. T., & Wechsler, R. H. 2014, *MNRAS*, **444**, 129
 Dai, B., & Seljak, U. 2021, *PNAS*, **118**, 2020324118
 Davies, L. J. M., Maraston, C., Thomas, D., et al. 2013, *MNRAS*, **434**, 296
 Davis, C., Rozo, E., Roodman, A., et al. 2018, *MNRAS*, **477**, 2196
 DeRose, J., Becker, M. R., & Wechsler, R. H. 2021a, arXiv:2105.12104
 DeRose, J., Wechsler, R. H., Becker, M. R., et al. 2019a, arXiv:1901.02401
 DeRose, J., Wechsler, R. H., Becker, M. R., et al. 2021b, arXiv:2105.13547
 DeRose, J., Wechsler, R. H., Tinker, J. L., et al. 2019b, *ApJ*, **875**, 69
 DES Collaboration, Abbott, T. M. C., Adamow, M., et al. 2021, *ApJS*, **255**, 20
 Diemer, B., & Joyce, M. 2019, *ApJ*, **871**, 168
 Dietrich, J. P., Zhang, Y., Song, J., et al. 2014, *MNRAS*, **443**, 1713
 Dong, F., Pierpaoli, E., Gunn, J. E., & Wechsler, R. H. 2008, *ApJ*, **676**, 868
 Eke, V. R., Frenk, C. S., Baugh, C. M., et al. 2004, *MNRAS*, **355**, 769
 Erickson, B. M. S., Singh, R., & Evrard, A. E. 2012, in Proc. of the 1st Conf. of the Extreme Science and Engineering Discovery Environment: Bridging from the eXtreme to the campus and beyond, XSEDE '12 (New York: ACM), 34
 Farahi, A., Evrard, A. E., Roza, E., Rykoff, E. S., & Wechsler, R. H. 2016, *MNRAS*, **460**, 3900

- Feng, Y., Chu, M.-Y., Seljak, U., & McDonald, P. 2019, FastPM: Scaling N-body Particle Mesh solver, Astrophysics Source Code Library, ascl:1905.010
- Fosalba, P., Crocce, M., Gaztañaga, E., & Castander, F. J. 2015, *MNRAS*, **448**, 2987
- Friedrich, O., Gruen, D., DeRose, J., et al. 2018, *PhRvD*, **98**, 023508
- Gatti, M., Giannini, G., Bernstein, G. M., et al. 2022, *MNRAS*, **510**, 1223
- Gatti, M., Vielzeuf, P., Davis, C., et al. 2018, *MNRAS*, **477**, 1664
- Gerdes, D. W., Sypniewski, A. J., McKay, T. A., et al. 2010, *ApJ*, **715**, 823
- Gerke, B. F., Wechsler, R. H., Behroozi, P. S., et al. 2013, *ApJS*, **208**, 1
- Gill, M. S. S., Young, J. C., Draskovic, J. P., et al. 2009, arXiv:0909.3856
- Gruen, D., Friedrich, O., Krause, E., et al. 2018, *PhRvD*, **98**, 023507
- Guo, Q., White, S., Angulo, R. E., et al. 2013, *MNRAS*, **428**, 1351
- Hansen, S. M., Sheldon, E. S., Wechsler, R. H., & Koester, B. P. 2009, *ApJ*, **699**, 1333
- Hao, J., McKay, T. A., Koester, B. P., et al. 2010, *ApJS*, **191**, 254
- Harnois-Déraps, J., Amon, A., Choi, A., et al. 2018, *MNRAS*, **481**, 1337
- Hearin, A., Korytov, D., Kovacs, E., et al. 2020, *MNRAS*, **495**, 5040
- Hearin, A. P., & Watson, D. F. 2013, *MNRAS*, **435**, 1313
- Hearin, A. P., Watson, D. F., Becker, M. R., et al. 2014, *MNRAS*, **444**, 729
- High, F. W., Hoekstra, H., Leethochawalit, N., et al. 2012, *ApJ*, **758**, 68
- Hoyle, B., Gruen, D., Bernstein, G. M., et al. 2018, *MNRAS*, **478**, 592
- Izard, A., Fosalba, P., & Crocce, M. 2018, *MNRAS*, **473**, 3051
- Jarrett, T. H., Cohen, M., Masci, F., et al. 2011, *ApJ*, **735**, 112
- Jarvis, M. J., Bonfield, D. G., Bruce, V. A., et al. 2013, *MNRAS*, **428**, 1281
- Jiang, F., Dekel, A., Freundlich, J., et al. 2021, *MNRAS*, **502**, 621
- Jiang, F., & van den Bosch, F. C. 2016, *MNRAS*, **458**, 2848
- Jing, Y. P. 1998, *ApJ*, **503**, L9
- Kauffmann, G., White, S. D. M., & Guiderdoni, B. 1993, *MNRAS*, **264**, 201
- Kitaura, F.-S., Rodríguez-Torres, S., Chuang, C.-H., et al. 2016, *MNRAS*, **456**, 4156
- Knebe, A., Knollmann, S. R., Muldrew, S. I., et al. 2011, *MNRAS*, **415**, 2293
- Koester, B. P., McKay, T. A., Annis, J., et al. 2007a, *ApJ*, **660**, 239
- Koester, B. P., McKay, T. A., Annis, J., et al. 2007b, *ApJ*, **660**, 221
- Korytov, D., Hearin, A., Kovacs, E., et al. 2019, *ApJS*, **245**, 26
- Krause, E., Eifler, T. F., Zuntz, J., et al. 2017, arXiv:1706.09359
- Kravtsov, A. V., Berlind, A. A., Wechsler, R. H., et al. 2004, *ApJ*, **609**, 35
- Kravtsov, A. V., Vikhlinin, A. A., & Meshcheryakov, A. V. 2018, *AstL*, **44**, 8
- Landy, S. D., & Szalay, A. S. 1993, *ApJ*, **412**, 64
- Lehmann, B. V., Mao, Y.-Y., Becker, M. R., Skillman, S. W., & Wechsler, R. H. 2017, *ApJ*, **834**, 37
- Leistedt, B., Peiris, H. V., Elsner, F., et al. 2016, *ApJS*, **226**, 24
- Lewis, A. 2004, *PhRvD*, **70**, 043011
- MacCrann, N., DeRose, J., Wechsler, R. H., et al. 2018, *MNRAS*, **480**, 4614
- Malz, A. I., Marshall, P. J., DeRose, J., et al. 2018, *AJ*, **156**, 35
- Mandelbaum, R., Seljak, U., Kauffmann, G., Hirata, C. M., & Brinkmann, J. 2006, *MNRAS*, **368**, 715
- Manera, M., Scoccimarro, R., Percival, W. J., et al. 2013, *MNRAS*, **428**, 1036
- Mao, Y.-Y., Kovacs, E., Heitmann, K., et al. 2018, *ApJS*, **234**, 36
- Mao, Y.-Y., Williamson, M., & Wechsler, R. H. 2015, *ApJ*, **810**, 21
- Martens, D., Fang, X., Troxel, M. A., et al. 2019, *MNRAS*, **485**, 211
- Masaki, S., Lin, Y.-T., & Yoshida, N. 2013, *MNRAS*, **436**, 2286
- Massara, E., Ho, S., Hirata, C. M., et al. 2021, *MNRAS*, **508**, 4193
- McMahon, R. G., Banerji, M., Gonzalez, E., et al. 2013, *Msngr*, **154**, 35
- Merson, A. I., Baugh, C. M., Helly, J. C., et al. 2013, *MNRAS*, **429**, 556
- Miller, C. J., Nichol, R. C., Reichart, D., et al. 2005, *AJ*, **130**, 968
- Modi, C., Feng, Y., & Seljak, U. 2018, *JCAP*, **2018**, 028
- Monaco, P., Sefusatti, E., Borgani, S., et al. 2013, *MNRAS*, **433**, 2389
- Moster, B. P., Macciò, A. V., Somerville, R. S., Naab, T., & Cox, T. J. 2011, *MNRAS*, **415**, 3750
- Moster, B. P., Naab, T., & White, S. D. M. 2018, *MNRAS*, **477**, 1822
- Myles, J., Alarcon, A., Amon, A., et al. 2021, *MNRAS*, **505**, 4249
- Myles, J., Gruen, D., Mantz, A. B., et al. 2021, *MNRAS*, **505**, 33
- Navarro, J. F., Frenk, C. S., & White, S. D. M. 1996, *ApJ*, **462**, 563
- Nord, B., Amara, A., Réfrégier, A., et al. 2016, *A&C*, **15**, 1
- Pandey, S., Baxter, E. J., Xu, Z., et al. 2019, *PhRvD*, **100**, 063519
- Park, Y., Krause, E., Dodelson, S., et al. 2016, *PhRvD*, **94**, 063533
- Ramanah, D. K., Lavaux, G., Jasche, J., & Wandelt, B. D. 2019, *A&A*, **621**, A69
- Reddick, R. M., Wechsler, R. H., Tinker, J. L., & Behroozi, P. S. 2013, *ApJ*, **771**, 30
- Rozo, E., Rykoff, E., Koester, B., et al. 2011, *ApJ*, **740**, 53
- Rozo, E., Wechsler, R. H., Koester, B. P., et al. 2007a, arXiv:astro-ph/0703571
- Rozo, E., Wechsler, R. H., Koester, B. P., Evrard, A. E., & McKay, T. A. 2007b, arXiv:astro-ph/0703574
- Rykoff, E. S., Rozo, E., Busha, M. T., et al. 2014, *ApJ*, **785**, 104
- Rykoff, E. S., Rozo, E., & Keisler, R. 2015, arXiv:1509.00870
- Safonova, S., Norberg, P., & Cole, S. 2021, *MNRAS*, **505**, 325
- Saito, S., Leauthaud, A., Hearin, A. P., et al. 2016, *MNRAS*, **460**, 1457
- Sánchez, C., Clampitt, J., Kovacs, A., et al. 2017, *MNRAS*, **465**, 746
- Saunders, W., Smedley, S., Gillingham, P., et al. 2014, *Proc. SPIE*, **9150**, 915023
- Schmidt, S. J., Malz, A. I., Soo, J. Y. H., et al. 2020, *MNRAS*, **499**, 1587
- Scoccimarro, R., & Sheth, R. K. 2002, *MNRAS*, **329**, 629
- Seljak, U. 2000, *MNRAS*, **318**, 202
- Sheldon, E. S., Johnston, D. E., Masjedi, M., et al. 2009, *ApJ*, **703**, 2232
- Shin, T., Adhikari, S., Baxter, E. J., et al. 2019, *MNRAS*, **487**, 2900
- Smith, A., Cole, S., Baugh, C., et al. 2017, *MNRAS*, **470**, 4646
- Soares-Santos, M., de Carvalho, R. R., Annis, J., et al. 2011, *ApJ*, **727**, 45
- Somerville, R. S., Olsen, C., Yung, L. Y. A., et al. 2021, *MNRAS*, **502**, 4858
- Somerville, R. S., & Primack, J. R. 1999, *MNRAS*, **310**, 1087
- Sousbie, T., Courtois, H., Bryan, G., & Devriendt, J. 2008, *ApJ*, **678**, 569
- Springel, V., White, S. D. M., Jenkins, A., et al. 2005, *Natur*, **435**, 629
- Stein, G., Alvarez, M. A., Bond, J. R., van Engelen, A., & Battaglia, N. 2020, *JCAP*, **2020**, 012
- Sutherland, W. 2012, in Science from the Next Generation Imaging and Spectroscopic Surveys (Garching: European Southern Observatory), **40**
- Szepietowski, R. M., Bacon, D. J., Dietrich, J. P., et al. 2014, *MNRAS*, **440**, 2191
- Tassev, S., Zaldarriaga, M., & Eisenstein, D. J. 2013, *JCAP*, **2013**, 036
- Tinker, J. L., Sheldon, E. S., Wechsler, R. H., et al. 2012, *ApJ*, **745**, 16
- To, C.-H., Krause, E., Rozo, E., et al. 2021, *MNRAS*, **502**, 4093
- To, C.-H., Reddick, R. M., Rozo, E., Rykoff, E., & Wechsler, R. H. 2020, *ApJ*, **897**, 15
- Tröster, T., Ferguson, C., Harnois-Déraps, J., & McCarthy, I. G. 2019, *MNRAS*, **487**, L24
- Troxel, M. A., MacCrann, N., Zuntz, J., et al. 2018, *PhRvD*, **98**, 043528
- Vale, A., & Ostriker, J. P. 2004, *MNRAS*, **353**, 189
- Vale, A., & Ostriker, J. P. 2006, *MNRAS*, **371**, 1173
- van den Bosch, F. C., & Ogiya, G. 2018, *MNRAS*, **475**, 4066
- van den Bosch, F. C., Ogiya, G., Hahn, O., & Burkert, A. 2018, *MNRAS*, **474**, 3043
- van den Bosch, F. C., Yang, X., Mo, H. J., et al. 2007, *MNRAS*, **376**, 841
- VanderPlas, J. T., Connolly, A. J., Jain, B., & Jarvis, M. 2012, *ApJ*, **744**, 180
- Varga, T. N., DeRose, J., Gruen, D., et al. 2019, *MNRAS*, **489**, 2511
- Vogelsberger, M., Marinacci, F., Torrey, P., & Puchwein, E. 2020, *NatRP*, **2**, 42
- Watson, D. F., Hearin, A. P., Berlind, A. A., et al. 2015, *MNRAS*, **446**, 651
- Wechsler, R. H. 2004, in Clusters of Galaxies: Probes of Cosmological Structure and Galaxy Evolution, ed. J. S. Mulchaey, A. Dressler, & A. Oemler (Pasadena, CA: Carnegie Observatories)
- Wechsler, R. H., & Tinker, J. L. 2018, *ARA&A*, **56**, 435
- Weinberg, D. H., Mortonson, M. J., Eisenstein, D. J., et al. 2013, *PhR*, **530**, 87
- Wetzell, A. R., & White, M. 2010, *MNRAS*, **403**, 1072
- White, M., Tinker, J. L., & McBride, C. K. 2014, *MNRAS*, **437**, 2594
- White, S. D. M., & Frenk, C. S. 1991, *ApJ*, **379**, 52
- Yamamoto, M., Masaki, S., & Hikage, C. 2015, arXiv:1503.03973
- Yan, R., White, M., & Coil, A. L. 2004, *ApJ*, **607**, 739
- Yang, S., Du, X., Benson, A. J., Pullen, A. R., & Peter, A. H. G. 2020, *MNRAS*, **498**, 3902
- Yang, X., Mo, H. J., & van den Bosch, F. C. 2003, *MNRAS*, **339**, 1057
- Zehavi, I., Zheng, Z., Weinberg, D. H., et al. 2011, *ApJ*, **736**, 59
- Zhang, X., Wang, Y., Zhang, W., et al. 2019, arXiv:1902.05965
- Zheng, Z., Berlind, A. A., Weinberg, D. H., et al. 2005, *ApJ*, **633**, 791
- Zheng, Z., Coil, A. L., & Zehavi, I. 2007, *ApJ*, **667**, 760
- Zu, Y., & Mandelbaum, R. 2015, *MNRAS*, **454**, 1161